Development of genetically-encoded fluorescent KSR1-based probes to track ceramides during phagocytosis

Vladimir Girik[1], Larissa van Ek[2,3], Isabelle Dentand Quadri[1], Maral Azam[1], Maria Cruz Cobo[1], Marion Mandavit[1], Isabelle Riezman[4], Howard Riezman[4], Anne-Claude Gavin[2,3,4], Paula Nunes-Hasler[1].

[1]Department of Pathology and Immunology, Geneva Center for Inflammation Research, Faculty of Medicine, University of Geneva, Geneva Switzerland

[2]Department of Cellular Physiology and Metabolism, Faculty of Medicine, University of Geneva, Geneva Switzerland

[3]Diabetes Center, Faculty of Medicine, University of Geneva, Geneva, Switzerland

[4]Department of Biochemistry, NCCR Chemical Biology, Faculty of Science, University of Geneva, Geneva Switzerland

***Corresponding Author:**

Paula Nunes-Hasler
Department of Pathology and Immunology
Geneva Center for Inflammation Research
Faculty of Medicine
University of Geneva,
1 Rue Michel-Servet
Geneva Switzerland 1211
Paula.Nunes@unige.ch

Key words: kinase suppressor of ras 1, SET nuclear proto-oncogene, I2PP2A, protein kinase c zeta, PRKCZ, C6-ceramide, sphingomyelinase, myriocin, fumonisin B1, stromal interaction molecule 1, Sec22b, lipidomics

Abstract

Ceramides regulate phagocytosis, however their exact function remains poorly understood. Here we sought 1) to develop genetically encoded fluorescent tools for imaging ceramide, and 2) to use them to examine ceramide dynamics during phagocytosis. Fourteen EGFP fusion constructs based on four known ceramide-binding domains were generated and screened. While most constructs localized to the nucleus or cytosol, three based on the CA3 ceramide-binding domain of KSR1 localized to plasma membrane or endolysosomes. C-terminally-tagged CA3 with a vector-based (C-KSR) or glycine-serine linker (C-KSR-GS) responded sensitively and similarly to ceramide depletion and accumulation using a panel of ceramide modifying drugs, whereas N-terminally tagged CA3 (N-KSR) responded differently to a subset of treatments. Lipidomic and liposome microarray analysis suggested that, instead, N-KSR preferentially binds to glucosyl-ceramide. Additionally, the three probes showed distinct dynamics during phagocytosis. Despite partial lysosomal degradation, C-KSR robustly accumulated at the plasma membrane during phagocytosis, whereas N-KSR becomes cytoplasmic at later timepoints. Moreover, weak recruitment of C-KSR-GS to endoplasmic reticulum and phagosomes was enhanced by overexpression of the endoplasmic reticulum proteins STIM1 and Sec22b, and was more salient in dendritic cells. The data suggest these novel probes can be used to analyze sphingolipid dynamics and function in living cells.

Introduction

Phagocytosis is a fundamental process whereby external foreign particles are internalized by cells, and the resulting membrane-engulfed compartment, called the phagosome, undergoes a series of maturation steps that lead to the formation of the digestive milieu and degradation of the foreign material (Levin et al.). A large body of literature has highlighted the central role of dynamic phosphoinositide lipid remodeling in controlling this process through the recruitment of a variety of effectors including cytoskeletal, motor or vesicular docking proteins that help guide phagosomes to their fate (Freeman and Grinstein; Levin et al.; Yeung and Grinstein). Sphingolipids are a diverse group of lipids crucial for maintaining cellular membrane structure, fluidity and curvature, that have long been recognized to additionally play bioactive signaling roles (Quinville et al.). Ceramides, a central hub of the sphingolipid network (Hannun and Obeid; Hannun and Obeid), have also been implicated in various steps of the phagocytic process. These span from facilitation of receptor clustering and activation (Avota et al.; Bakr et al.), to initial membrane deformation of phagocytic cups (Magenau et al.; Niekamp et al.), to promotion of phago-lysosome fusion (Hinkovska-Galcheva et al.; Schramm et al.; Wu et al.), and inhibition of antigen presentation in dendritic cells (Fuglsang et al.; Sallusto and Nicol). However, compared to phosphoinositides, less is known about the dynamics, regulation and roles of ceramide and its related lipids during this critical immune process (Saharan et al.).

Arguably, part of the challenge may lie in the difficulty tracking these lipids in living cells (Canals et al.). The most reliable methods such as mass spectrometry do not have the spatial resolution required for subcellular tracking (Buchberger et al.), or rely on labor, cost and material intensive organelle isolation that still suffer from contamination of endoplasmic reticulum (ER) membranes due to tightly tethered membrane contact sites (MCS) that may skew lipid content (Scorrano et al.). In addition, tools such as fluorescent sphingolipid analogs are rapidly metabolized and may partition in membranes in a different manner than their natural counterparts (Canals et al.). Moreover, permeabilization steps necessary for access of anti-ceramide antibodies to intracellular membranes such as phagosomes may disrupt natural lipid localization (Bjørnestad and Lund). Therefore, an alternative approach enabling detection of ceramide in living cells with high spatial resolution is desirable. Genetically encoded lipid probes, typically composed of lipid-binding domains coupled to a fluorescent tag, provide an opportunity to investigate subcellular localization, relative cytosolic accessibility, and dynamics in living cells, and have been extensively employed to dissect phospholipid dynamics during phagocytosis (Hammond et al.). A few described lipid probes specific for sphingolipids have been published (Bakrac et al.; Yamaji et al.). However, no fluorescent ceramide biosensor based on isolated ceramide-binding domains have been

86 described so far, although a range of full-length ceramide-binding proteins have been
87 characterized (Bidlingmaier et al.; Bockelmann et al.; Deng et al.; Zhou et al.). Yet, the
88 localization of these proteins, which are all multi-domain proteins, may be governed by
89 cooperative binding events including ceramide but also involving other factors or domains. An
90 *E. coli* purified glutathione-S-transferase-fusion of the CA3 ceramide-binding domain of the
91 pseudokinase KSR1 was used *in vitro* and demonstrated ceramide-binding specificity (Yin et
92 al.), yet fluorescent versions of this construct for expression in mammalian cells have not been
93 published. In the current report, we document the cloning and screening of 14 putative
94 ceramide-binding genetically encoded fluorescent probes. Out of several potential ceramide-
95 binding biosensors, three constructs all bearing the same CA3 domain of the human
96 pseudokinase KSR1 were characterized further. These were named N-KSR, C-KSR and C-
97 KSR-GS according to which terminal (amino, N-, or carboxy, C-) the fluorescent protein was
98 fused to, and the presence of a glycine-serine (GS) rich linker. The three KSR1-based probes
99 responded to treatments modifying ceramide levels in cells, although changes in both the
100 localization and global fluorescence levels differed between the three constructs depending
101 on the stimulus. Immunostaining, liposome microarray, lipidomic analyses together with
102 further testing of the cellular behavior of the probes indicated that: N-KSR may instead be
103 more sensitive to glycosylated ceramides, C-KSR is less stable than the other two probes,
104 and that both of these factors contributed to the differences in cellular responses observed.
105 Interestingly, differential localization between the three probes, depending on cell type and
106 expression of ER-localized constructs, were documented to occur during phagocytosis.
107 Together our data indicate that these constructs may be useful tools for dissecting subcellular
108 sphingolipid dynamics and warrant further characterization.

109

110 **Results**

111 **KSR1-based probes associate to cellular membranes**

112 In previous studies, ceramide has been reported to be present in multiple organelles,
113 including plasma membrane, ER, Golgi, mitochondria, lysosomes and nucleus (Adachi et al.;
114 Götz et al.; Krishnamurthy et al.; Ledeen and Wu; Walter et al.; Wang et al.). In artificial
115 membranes, ceramide, a relatively hydrophobic lipid, readily flip-flops across bilayers
116 (Contreras et al.; Pohl et al.), and although mechanisms that actively maintain bilayer
117 asymmetry of ceramides may exist, to our knowledge they have not been described. Thus,
118 the localization pattern of a ceramide-binding probe could conceivably include binding to
119 several different types of intracellular membranes. To identify ceramide-specific biosensors,
120 four domains that have been previously demonstrated to bind ceramides *in vitro* and/or *in vivo*

121 were selected: 1) the earmuff domain (EMD) of the human SET protein [amino acids (aa) 70-
122 226] (Mukhopadhyay et al.); 2) the N-terminal C1 domain of atypical human protein kinase C
123 zeta (PRKCZ, also called PKCζ), aa 123-193); 3) the C-terminal C20 domain (aa 405-646) of
124 the same protein PRKCZ (Wang et al.; Wang et al.); and 4) the CA3 domain (also called C1
125 or cysteine-rich domain, aa 317-400) of the human pseudokinase KSR1 (Yin et al.) (Fig 1A).
126 The selected domains were tagged with EGFP at the amino or carboxy terminus (prefixed with
127 N- and C- respectively) and expressed in mouse embryonic fibroblasts (MEFs). Fusion
128 proteins based on SET (Fig 1Bi-ii) and PRKCZ (Fig 1Ci-iv) were primarily localized to the
129 nucleus. A nuclear export signal (NES) was added to C-SET-EMD (Fig 1Biii) and C-PRKCZ-
130 C20 (Fig 1Cv) to release proteins trapped in the nucleus, a strategy previously used for other
131 lipid biosensors (Goulden et al.). C-NES-PRKCZ-C20 and C-NES-SET-EMD were mainly
132 found in the cytosol, though nuclear localization was still noticeable (Fig 1Biii, 1Cv). In contrast,
133 the expression pattern of KSR1-based constructs depended on the position of the fluorescent
134 tag and linker (Fig 1D). N-terminally-tagged KSR1-CA3 domain (N-KSR) was found primarily
135 at the plasma membrane (Fig Di), while the C-terminally tagged probe (C-KSR) localized to
136 large intracellular vesicles (Fig 1Dii). Examination of the vector-based linker in C-KSR
137 revealed the introduction of a degradation signal RLELKLRILQ (Majeski and Fred Dice), and
138 Western blot as well as immunostainings with organelle markers transferrin, Rab7 and LAMP1
139 confirmed partial targeting to lysosomes and degradation (Fig S1A-C). Thus, a C-terminally
140 tagged construct with an alternate glycine-serine (GS)-rich linker was also generated and
141 abbreviated C-KSR-GS (Fig 1Diii). This construct displayed a localization similar to N-KSR,
142 although the plasma membrane localization was only salient in a subset of cells, and was
143 more stable than C-KSR (Fig 1Di, 1Diii, Fig S1D). To potentially increase the lipid biosensor
144 affinity (Hammond et al.), a construct expressing two KSR1 CA3 domains in tandem fused at
145 the C-terminus to EGFP was also generated (abbreviated 2X-C-KSR). However, the
146 localization appeared similar to that of C-KSR-GS (Fig 1Div). The localization of both N- and
147 C-KSR constructs depended on two conserved cysteines (C359/C362) whose mutation to
148 serine has previously been shown to decrease ceramide binding *in vitro.* This suggests that
149 their subcellular location might indeed involve ceramide binding (Yin et al.) (Fig 1Dv-vi). When
150 expressed in human Hela cells, probes based on KSR1, SET, and PRKCZ probes show a
151 subcellular localization patterns similar to that seen in MEFs (Fig S2) confirming the idea that
152 they can function similarly in different cellular contexts. Since phagosomal membranes are
153 derived from the plasma membrane and eventually fuse with lysosomes (Levin et al.), we
154 selected three of the KSR1-based probes that showed salient association to such cellular
155 membranes for further characterization: N-KSR, C-KSR and C-KSR-GS. Stable MEF cell lines
156 for N-KSR and C-KSR were successfully generated and employed in subsequent
157 experiments, while C-KSR-GS was characterized by transient transfection.

158 **KSR-based probes respond to sphingolipid depletion**

159 Next, the behavior of the three KSR probes in response to changes in cellular ceramide
160 levels was investigated. To induce ceramide depletion, cells were exposed to well-known
161 inhibitors of sphingolipid biosynthesis: myriocin, a potent inhibitor of serine-
162 palmitoyltransferase (Miyake et al.), the enzyme which catalyzes the first step in sphingolipid
163 biosynthesis; and fumonisin B1, a selective inhibitor of ceramide synthases (Merrill et al.).
164 Upon ceramide depletion, C-KSR-expressing cells demonstrated a drastic 5-fold decrease in
165 the intracellular fluorescence after a 3-day incubation with myriocin (0.5 μM) or fumonisin B1
166 (2.5 μM), accompanied by some re-localization to the cytosol in a subset of cells (Fig 2A-B).
167 In comparison, only a 2.5-fold decrease in the probe intensity was observed in N-KSR
168 expressing cells after sphingolipid depletion with either drug (Fig 2C-D). Targeted quantitative
169 tandem mass-spectrometry lipidomic analysis (Guri et al.) confirmed that total levels of all
170 major sphingolipid classes measured including ceramides, glycosylated ceramides
171 (comprising glucosyl and galactosyl ceramides of identical mass, collectively termed hexosyl-
172 ceramides) and sphingomyelins, were markedly depleted by myriocin treatment (Fig 2E, see
173 also Supplementary Data S1). In contrast, total levels of phospholipid species
174 phosphatidylcholine (PC), phosphatidylethanolamine (PE), phosphatidylserine (PS) and
175 phosphoinositide (PI) were unchanged (Fig 2E). In addition, myriocin treatment of cells
176 transiently transfected with C-KSR and cytosolic TagRFP did not produce any noticeable
177 effect on TagRFP expression (Fig S3), confirming a specific effect of myriocin on KSR
178 constructs. In contrast, although no signs of toxicity were noted upon transient transfection of
179 C-KSR-GS alone, 3-day treatment with myriocin or fumonisin B1 of these cells was toxic,
180 precluding analysis. However, overnight treatment with 10 μM fumonisin B1 also resulted in a
181 2-fold decrease in global cellular expression of C-KSR-GS (Fig 2F-G), indicating that similar
182 to both N-KSR and C-KSR, C-KSR-GS responds to sphingolipid depletion.

183

184 **KSR-based probes react differently to ceramide accumulation**

185 To induce ceramide accumulation at different subcellular locations, two methods were
186 employed. In the first, treatment with the ceramide precursor 16 carbon acyl-chain (C16) fatty
187 acid palmitate for 4h was used to increase ceramide via *de novo* biosynthesis (Kiefer et al.;
188 Tran et al.), which would be expected to increase ceramide in the ER where biosynthesis
189 takes place as well as potentially in the secretory pathway (Hannun and Obeid). In the second,
190 cells were incubated for 30 min with purified bacterial sphingomyelinase from *Staphylococcus*
191 *aureus* (SMase), which increases plasma membrane ceramides directly by hydrolyzing the
192 choline-ceramide derivative sphingomyelin on the outer leaflet of the plasma membrane, and

193 could potentially increase ceramides additionally within the endocytic system (Abe and
194 Kobayashi; Devaux). Palmitate treatment led to a 3-fold and 1.5-fold increase in global C-KSR
195 and C-KSR-GS signal intensity, respectively, without an obvious shift in subcellular
196 localization (Fig 3A, 3B). This was in contrast to the N-KSR probe which did not show any
197 changes in fluorescence intensity or localization (Fig 3C). Lipidomic analysis confirmed that
198 palmitate treatment induced a 2-fold accumulation of total ceramides, driven by the 4-fold
199 increase in C16-ceramide (Fig 3D, see also Supplementary Data S1). On the other hand,
200 palmitate did not induce changes in total hexosyl-ceramides, nor in total PC, PE and PI (Fig
201 3D). However, unexpectedly, depletion of the following were noted: total sphingomyelin, driven
202 by decreased C18- and C24-sphingomyelin; C24-hexosyl-ceramide, and total PS (Fig 3D, Di-
203 iii).

204 Next, the two C-terminally tagged constructs C-KSR and C-KSR-GS which showed
205 only partial plasma membrane localization under resting conditions were examined for their
206 response to treatment with SMase (0.5 U/ml) for 30 min (Fig 4A). This led both to a small but
207 significant increase in global C-KSR fluorescence intensity (Fig 4B) as well as to a robust 2-
208 fold increase in the recruitment of C-KSR to the plasma membrane (Fig 4A inset, 4C),
209 measured as the fraction of cells displaying plasma membrane localization in SMase treated
210 cells compared to PBS-treated controls (Fig 4C). A significant 1.5-fold increase in the fraction
211 of cells displaying plasma membrane localization of C-KSR-GS was also observed (Fig 4D-
212 E), whereas analysis of N-KSR was not conducted since nearly all cells displayed plasma
213 membrane localization at resting conditions. Lipidomic analysis revealed that SMase induced
214 a dramatic 20-fold accumulation of total ceramide species (Fig 4F), driven by increased C16-
215 ceramide (Fig 4Fii, see also Supplementary Data S1). Total hexosyl-ceramides were not
216 different but an increase in very short-chain C10-hexosyl-ceramides, a lipid species of
217 unknown biological significance, was observed (Fig 4F, Fii). Although total sphingomyelin was
218 not significantly different (Fig 4F), reductions in long-chain C22- and C24-sphingomyelin were
219 observed confirming efficient cleavage of longer-chain species (Fig 4Fii). That cleavage of
220 sphingomyelin was efficient was additionally assessed by staining with a purified EGFP-
221 tagged sphingomyelin-specific probe lysenin (20 µg/ml) (Kwiatkowska et al.), which was lost
222 upon SMase treatment (Fig S4A). Diacylglycerol (DAG) is a molecule with close structural
223 similarity to ceramide that could potentially be indirectly generated by activation of SM
224 synthases upon large increases of ceramide such as those observed under SMase treatment
225 here (Ekman et al.; Goñi and Alonso). Thus, the specificity of C-KSR for ceramide was further
226 investigated by generation of C-KSR-mRFP and co-expression with the DAG probe GFP-
227 PKC-C1(2) (Codazzi et al.). Cells were then treated with either 10 µM ionomycin (Iono) for 10
228 min, in order to induce plasma membrane DAG accumulation (Botelho et al.) or with SMase

229 as above. Whereas ionomycin treatment but not SMase induced PKC-C1(2) plasma
230 membrane recruitment, the opposite pattern was observed for C-KSR (Fig 4G-H). Treatment
231 with SMase did not affect the localization of PKC-C1(2) when it was expressed alone, nor did
232 it affect the localization of an alternate DAG probe YFP-DBD (Gallegos et al.) (Fig S4C), ruling
233 out potential indirect DAG accumulation after treatment with SMase. Collectively, the data
234 suggest that out of the three probes analyzed, C-KSR is the most sensitive to the changes in
235 cellular levels of ceramides and can also detect locally generated ceramides at the plasma
236 membrane, and that C-KSR-GS responds similarly to C-KSR but with a smaller dynamic
237 range. Most importantly, the lack of response of N-KSR to palmitate suggests a potential
238 difference in lipid binding specificity.

239

240 **N-KSR binds glucosyl-ceramide**

241 To further investigate the mechanism underlying the differences in how the KSR-based
242 probes react to ceramide accumulation, we sought to measure their *in vitro* binding specificity
243 to artificial membranes containing different ceramide species and derivatives. To this end, a
244 liposome microarray-based assay (LiMA) was employed, where arrays of liposomes (small
245 artificial vesicles) of various compositions are deposited inside a microfluidic chip, exposed to
246 purified (or cell lysates containing) fluorescent lipid-binding probes, and binding is assessed
247 by automated fluorescence microscopy (Saliba et al.). To obtain purified probes, the N-KSR
248 and C-KSR probes were re-cloned into super-folding GFP (sfGFP) bacterial expression
249 vectors (Pédelacq et al.) and purified from *E.coli* cultures. Interestingly, significant binding of
250 N-KSR was observed to dioleoyl-phosphatidylcholine (DOPC) liposomes containing 2%
251 glucosyl-ceramide (GlcCer), whereas the trends toward binding to liposomes containing either
252 10% sphingomyelin or 10% bovine ceramide mixtures were not significant (Fig 5A, Fig S5A,
253 see also Supplementary Data S2). Purified C-KSR tended to aggregate in this assay, and the
254 sample sizes were too small to allow individual statistical analysis of the different membrane
255 types. However, comparison of the binding scores of control liposomes versus those
256 containing 10% ceramide or ceramide derivatives suggests a preference for the latter (Fig 5B).
257 We also studied the binding of C-KSR-GS expressed in lysates from transfected HEK293
258 cells, to ceramide present in liposomes with either DOPC as the carrier lipid, or in liposomes
259 based on palmitoyl-oleoyl-PC (POPC) that mimic the composition of the inner plasma
260 membrane (IPM liposomes) (Lorent et al.) (Fig 5C, S5C-D). Lysates from HEK cells
261 expressing soluble EGFP and the DAG probe PKC-C1(2) were employed as negative and
262 positive controls, respectively (Fig S5D). Whereas robust and significant binding of PKC-C1(2)
263 to DAG-containing liposomes as compared to IPM liposomes was readily observed (Fig S5D,

264 Supplementary Data S2), the trend for a difference in binding scores of C-KSR-GS to
265 individual ceramide containing liposome compositions as compared to controls (DOPC, POPC
266 or IPM only) alone were not significant (Supplementary Data S2). On the other hand, when
267 pooling liposome data to increase statistical power as above, a comparison of pooled control
268 liposome spots (DOPC, POPC and IPM alone) to DOPC or IPM liposomes containing 5% and
269 10% ceramides, a small, but significant difference in binding scores was observed in the IPM
270 context (Fig 5C). These data support a preference of C-KSR-GS for ceramide-containing
271 membranes within a more complex lipid context.

272 Since the *in vitro* conditions tested likely do not fully recapitulate the optimal conditions
273 for lipid binding of our probes, we continued our exploration of the differences between C- and
274 N-terminally tagged probes within the cellular context. Thus, we next examined the response
275 of the two probes displaying the most similar localization pattern (N-KSR and C-KSR-GS) to
276 additional reagents previously shown to increase cellular ceramides. To this end, cells
277 expressing either probe were treated for 2h with 200 μM of the ceramide analogue C6-
278 ceramide (Kjellberg et al.) or overnight with 200 μM of the glucosyl-ceramide synthase inhibitor
279 Genz-123346 (Zhao et al.) or their respective ethanol and methanol vehicle controls.
280 Previously, C6-ceramide has been shown to induce large increases in endogenous ceramides
281 and hexosyl-ceramides, with an only comparatively smaller increase in sphingomyelin (Duran
282 et al.; Kjellberg et al.; Vieu et al.). In contrast, Genz-123346 increased ceramide without
283 affecting sphingomyelin and concomitantly decreasing hexosyl-ceramides (Koike et al.; Zhao
284 et al.). Interestingly, whereas both probes showed a robust increase in cellular fluorescence
285 upon treatment with C6-ceramide (Fig 5E-H), a strikingly different response to Genz-123346
286 treatment was noted, where an increase in fluorescence was observed with C-KSR-GS but
287 not with N-KSR (Fig 5E-H). Together, these data suggest that a preference of N-KSR for
288 glucosyl-ceramide instead of ceramide could explain the difference in cellular behavior of the
289 N- and C-terminally tagged probes.

290

291 **KSR1-based probes behave differently during phagocytosis**

292 In several reports, ceramide generation has been associated with phagocytic ingestion
293 and phagosomal maturation, and shown to be important for pathogen elimination, yet its
294 precise role is still poorly understood (Pathak et al.; Tafesse et al.). Thus, to not only glean
295 some hints at ceramide dynamics (and eventually function) during this important immune
296 process, but also to test our probes under a physiological stimulus, we next investigated the
297 behavior of our three KSR1-based probes during phagocytosis. To this end, we examined
298 MEFs rendered phagocytic by overexpression of the FCGR2A-c-myc. This phagocytic cell

299 model is easier to transfect and manipulate than naturally phagocytic cells, and we and others
300 employing a similar strategy have observed such models recapitulate many aspects of the
301 phagocytic process, including phospholipid dynamics (Bodman-Smith et al.; Criado Santos et
302 al.; Giodini et al.; Hinkovska-Galcheva et al.). Cells expressing each of the three KSR1-based
303 probes (C-, N- and C-KSR-GS) were exposed to 3 µm IgG-opsonized polystyrene beads for
304 30 min or 135 min, time-points representative of early and late stages of phagosomal
305 maturation (Fig 6A-C). In parallel, sphingolipid levels were measured in C-KSR-expressing
306 cells using targeted lipidomics, where a large accumulation in total cellular ceramides,
307 sphingomyelin and hexosyl-ceramide (4-, 2.6- and 6-fold respectively) was observed at 30 min
308 (Fig 6D, see also Supplementary Data S1). This effect was driven by changes in C16- and
309 C24-ceramide, C24-sphingomyelin, and C16- as well as C24-hexosyl-ceramide species (Fig
310 6Di-ii). It should be noted that changes in total PC, PI and PS were also observed (Fig 6Diii-
311 iv). Interestingly, 30 min after the incubation with IgG-coupled beads, accumulation of C-KSR
312 at the plasma membrane, similar to what was observed after incubation with bacterial SMase,
313 was noted (Fig 6A, see also Fig 4A). Exploring this plasma membrane localization further, we
314 found that plasma membrane staining of C-KSR could still be detected at 45 min and 60 min
315 after phagocytosis initiation, yet was lost at later stages, after 90 and 135 min (Fig S6A).
316 Similarly, plasma membrane localization of N-KSR and C-KSR-GS was salient at 30 min (Fig
317 6B-C), even though both constructs were already found at the plasma membrane under basal
318 conditions, whereas at 135 min the global N-KSR signal was not as clearly discerned (Fig 6B).
319 Moreover, whereas N-KSR was completely absent from phagosomes (Fig 6B, insets), in C-
320 KSR-GS-expressing cells, accumulation around phagosomes was detected in a subset of
321 phagosomes (Fig 6C, arrows). In some instances, a pattern of small flattened cisternae or
322 protruding tubular structures could be seen around phagosomes, which were reminiscent of
323 membrane contact sites (MCS) between the phagosomal membrane and ER, structures that
324 have been studied extensively by our laboratory in the past (Criado Santos et al.; Guido et al.;
325 Nunes-Hasler et al.; Nunes et al.) (Fig 6C, arrows). To confirm whether such structures could
326 indeed represent ER, C-KSR-GS was then co-expressed with several ER-targeted constructs,
327 including: a soluble ER-targeted RFP TagRFP-KDEL, a calcium regulator and MCS marker
328 mCh-STIM1 and mCh-Sec22b, a protein regulating traffic between ER and Golgi that we have
329 recently shown to tether STIM1-independent MCS (Criado Santos et al.; Nunes et al.) (Figs
330 6E-F, Fig S6B). Interestingly, although overlap between C-KSR-GS and KDEL was not easily
331 discerned, likely due to low overall KDEL expression (Fig S6B), overlap between C-KSR-GS
332 and STIM1 as well as C-KSR-GS and Sec22b was observed in some but not all instances of
333 periphagosomal accumulation of the fluorescent proteins (Fig 6E-F). Finally, we expressed
334 the N-KSR and C-KSR-GS probes in a naturally phagocytic dendritic cell line JAWS II. Similar
335 to MEFs, N-KSR did not localize to the phagosomal or other organellar membranes and

336 appeared to be depleted at late phagocytic time points (Fig 7A). In contrast, robust C-KSR-
337 GS accumulation at the phagosomal membrane could be discerned on a subset of
338 phagosomes, as well as on internal structures reminiscent of the ER (Fig 7B). Together these
339 intriguing observations suggest the following: first, that the large changes in ceramide during
340 the first 30 min of phagocytosis detected in whole-cell MEF extracts are likely occurring at the
341 plasma membrane and are best detected by C-KSR which is the most sensitive of the three
342 probes at detecting changes of plasma membrane ceramides, whereas changes in glucosyl-
343 ceramide may be explored instead using the N-KSR probe. Secondly, C-KSR-GS may be
344 more useful to detect ceramide species on intracellular membranes including phagosomal and
345 ER membranes. Finally, the data also hint at dynamic ceramide fluxes, potentially at contact
346 sites between phagosomal membrane and ER.

347

348 **Discussion**

349 Despite several proteins reported as ceramide binders (Bockelmann et al.; Canals et
350 al.; Zhou et al.), to our knowledge no genetically encoded ceramide-specific probes per se
351 have been reported, though whole GFP-tagged ceramide-binding proteins were employed to
352 track subcellular ceramide in a limited number of studies (Canals et al.). Out of 14 candidate
353 biosensor constructs reported here, we focused on three based on the KSR1 CA3 (317-400)
354 ceramide-binding domain which displayed membrane localization when expressed in cells. In
355 contrast, constructs based on PRKCZ and SET were targeted to the nucleus, without obvious
356 association to cellular membranes. Since sphingolipids have been reported to be present in
357 both the nuclear membrane as well as nuclear matrix (Ledeen and Wu), and indeed SET has
358 a defined nuclear activity (Adachi et al.), it is possible that these proteins may detect ceramide
359 in the nuclear matrix rather than simply being misfolded (Albi and Viola Magni). Future studies
360 employing stimuli such as DNA damage, known to change nuclear ceramides may still help to
361 verify the utility of these constructs.

362 In contrast, though nuclear shuttling has also been reported for KSR1, this scaffolding
363 regulator of MAPK signaling normally resides in the cytosol in resting conditions (Brennan et
364 al.). It is recruited to the plasma membrane upon growth factor stimulation, which induces both
365 changes in phosphorylation of multiple KSR1 residues, as well as the activities of neutral and
366 acidic SMases, generating ceramide (Mathias et al.; Razidlo et al.). Thus KSR1-based probes
367 are particularly poised to detect ceramide in the context of plasma membrane lipids. The
368 baseline localization of N-KSR, 2x-C-KSR and C-KSR-GS, as well as recruitment to the
369 plasma membrane upon SMase treatment of C-KSR and C-KSR-GS are all consistent with
370 this notion. In addition to ceramide binding, mutagenesis studies suggest that phosphorylation

371 of T274 and S392 contribute to KSR1 stability. Notably, dephosphorylation of S392, a residue
372 found within the CA3 domain, participates in membrane re-localization upon growth factor
373 activation (Brennan et al.; Razidlo et al.). Whether S392 in the CA3 of our KSR constructs is
374 constitutively dephosphorylated, or whether separation from other KSR1 domains is sufficient
375 to allow conformational changes favoring ceramide binding remains to be defined. However,
376 full-length KSR1-S392A localizes to the nucleus rather than the plasma membrane (Brennan
377 et al.). Several studies have reported direct ceramide binding of the KSR1 CA3, including *in*
378 *vitro* reports using an N-terminal GST-fusion with a CA3 of similar composition (aa 320-388)
379 as in our own study (aa 317-400), though others, notably some employing a truncated CA3
380 (aa 334 to 377), have failed to detect direct binding (Pérez-rivas et al.; Yin et al.; Zhang et al.;
381 Zhou et al.). On the other hand, the structure of this truncated CA3 has been resolved and
382 shows a shallow ceramide binding pocket that was identified based on similarity to other C1
383 domains, involving residues L342, V345, M353, I354 and F355 (Zhou et al.). Thus, the KSR1
384 CA3 would not be expected to, on its own, interact with the fatty acid chain or to be able to
385 extract lipids from membranes, but rather to interact with lipid head-groups.

386 In the characterization of our probes, a surprising observation was that the most salient
387 change in the behavior of the KSR probes in response to ceramide-modifying drugs was a
388 change in total cellular fluorescence. This contrasts with similar phospholipid probes, which
389 usually change their locations rather than their total fluorescence. The effect was consistently
390 observed in both induction and depletion of ceramides and across all drug treatments tested
391 (Figs 2-5). For myriocin treatment, a simple toxicity effect (which often accompanies changing
392 levels of ceramide (Hannun and Obeid) was ruled out since levels of cytosolic RFP were
393 unchanged. In addition, with SMase treatment, neither the two DAG probes reacted in this
394 manner (Fig 4, S4). A potential explanation is that the CA3 domain itself is somewhat unstable
395 and subject to an intrinsic degradation that is mitigated by membrane binding. Indeed, full-
396 length KSR1 binds cytosolic chaperones Hsp70, 90 and 68, (Stewart et al.), and KSR1 is
397 ubiquitinated, though at a site outside the CA3 domain (Matheny et al.; Rinaldi et al.).
398 Moreover, phosphorylation at both T274 and S392 increases the half-life of KSR1 from 1hr to
399 6hr (Rinaldi et al.). Such a fast turnover time is consistent with our results which were observed
400 even with treatments as short as 30 min. A requirement for turnover time may also explain
401 why a smaller increase in total fluorescence was observed with the shorter SMase treatment,
402 despite the fact that changes in total ceramides were larger. However, whether
403 phosphorylation, ubiquitination, or chaperone binding might also be modified, increasing
404 stability also of the cytosolic fraction of the probe, will be important to define in future studies.

405 In addition to its potential influence on cellular probe behavior, an intrinsic instability,
406 or requirement for post-translational modification of the CA3 domain to prevent aggregation

407 or precipitation in solution, and increase ceramide binding efficiency, could well explain the
408 weak though detectable *in vitro* binding observed for C-KSR-GS and C-KSR to artificial
409 membranes containing ceramide or ceramide-derivates. Nevertheless, a significant and
410 surprising interaction of the N-KSR probe to glucosyl-ceramide-containing liposomes was
411 observed. Though unexpected, such a modification to the lipid specificity of the CA3 domain
412 is consistent with the difference in behavior between N- and C- constructs to palmitate, Genz-
413 123346 as well as to phagocytic stimuli. Future studies with drugs or genetic manipulation of
414 enzymes such as glucosyl and galactosyl ceramidases or transporters such as TMEM16F
415 (Suzuki et al.) would be useful to corroborate these finding and determine more precisely the
416 specificity of this probe for glycosylated or potentially phosphorylated ceramides in the cellular
417 context. In addition, it would be worth to explore whether, for example, the creation of S392A
418 mutants of the C-KSR-GS construct, which lacks MEK-interaction domains that leads to
419 nuclear localization (Brennan et al.), may improve probe stability in solution, allowing *in vitro*
420 ceramide-binding to be more robust. Overall, the examination of our three KSR1-based probes
421 under different stimuli (summarized in Fig 8) demonstrated that these probes may each have
422 their own utility as such or serve as a basis for future designs and studies aimed at dissecting
423 ceramide, and potentially glucosyl-ceramide, dynamics in cells. The exacerbated instability of
424 C-KSR, which prevented constitutive plasma membrane localization, proved in fact to be
425 advantageous in the way that it allowed for a greater dynamic range and more salient plasma
426 membrane recruitment with a phagocytic stimulus than C-KSR-GS. Thus, like conditional
427 instability employed in nanobody engineering (Tang et al.), a future design could build upon
428 these observations to include proteasome targeting signals, which may be less disruptive than
429 the current design to membrane homeostasis (Zhao et al.), to obtain a sensitive on-off
430 biosensor for plasma membrane ceramide.

431 Finally, our intriguing observations of the differential behavior of N-KSR and C-KSR-
432 GS during phagocytosis further support the notion that these two very similar probes are
433 responding to different lipid changes in the cell. One important notion to consider is that such
434 cytosolic probes will only detect lipids that are present on the cytosolic leaflet, or when luminal
435 leaflets are exposed to the cytosol for example during plasma membrane or lysosomal
436 disruption. Indeed, the sphingomyelin probe lysenin has recently contributed greatly to our
437 understanding of the role of sphingomyelin (and indirectly ceramide) in membrane repair and
438 antigen cytosol transfer in dendritic cells (Canton et al.; Childs et al.; Niekamp et al.). Though
439 several studies indicate that ceramide readily flip-flops across lipid bilayers (Contreras et al.;
440 Goñi et al.; Pohl et al.), this is not so for complex sphingolipids such as glucosyl-ceramide,
441 where trans-bilayer transporters might maintain or establish gradients in response to cellular
442 signals as occurs for PS (Suzuki et al.; Williamson). Changes such as the loss of the N-KSR

443 signal might equally represent a loss of total glucosyl-ceramide as it might simply reflect its
444 removal from the cytosolic leaflet, which could explain why global changes in hexosyl-
445 ceramides was not detected by lipidomic analysis, though compensating changes in
446 galactosyl-ceramide could also provide an explanation. However, that the exciting ER
447 localization of C-KSR-GS upon certain conditions is simply a result of misfolding is unlikely,
448 and investigation of whether this truly represents ceramide flux is ongoing in our laboratory.
449 Although clearly more work will be required to define the behavior and lipid specificity of these
450 novel biosensors, we believe these constructs represent useful new tools to explore
451 sphingolipid regulation and function in living cells.

452

453 **Materials and Methods**

454 *Reagents*

455 The following antibodies (antibody Name/catalog #/dilution) were from: Abcam (USA)
456 – anti-Rab7/ ab137029/1:100; anti-Rab5/ab18211/1:100; Enzo Life Sciences (USA) – anti-
457 LAMP1/ ADI-VAM-EN001/1:50, BD Biosciences (USA) – anti-TGN38/ 610898 /1:200; Thermo
458 - AF555 Goat anti-mouse IgG/ A-21422/1:500, AF555-goat-anti-rabbit IgG/A-21428/1:250;
459 Santa-Cruz Biotechnology - Goat anti-rabbit IgG-HRP/1:5000, BioRad (USA) – Goat anti-
460 mouse IgG-HRP/170-6516/1:3000. All lipid standards for lipidomic analysis were from Avanti
461 (Sigma/Merck) amounts given per 6-cm cell culture dish: DLPC (12:0-12:0 PC, 0.4 nmol/dish,
462 cat. #850335), PE31:1 (17:0-14:1 PE, 1 nmol/dish, cat # LM-1104), PI31:1 (17:0-14:1 PI, 1
463 nmol/dish, cat # LM-1504), PS31:1 (17:0-14:1 PS, 3.3 nmol/dish, cat# LM-1304), CL56:0 (14:0
464 Cardiolipin, 0.7 nmol/dish, cat#710332), C12SM (C12 Sphingomyelin d18:1-12:0, 0.1
465 nmol/dish, cat#860583), C17Cer (C17 Ceramide, d18:1-17:0, 2.5 nmol/dish, cat #860517),
466 C8GC (C8 Glucosyl(B)Ceramide, d18:1-8:0, 0.5 nmol/dish, cat#860540). Lipids employed in
467 the liposome microarray analysis are listed in Supplementary Table S1. Chemicals were
468 purchased from Sigma/Merck unless otherwise stated, (Name/catalog #): HPLC grade
469 Methanol/4860-1L-R, HPLC grade Chloroform/650471, tert-Butyl Methyl Ether
470 (MTBE)/650560, Methylamine/534102; LC-MS grade water/1153331000. Thermo: HPLC
471 grade n-butanol/11378197. Plasmids used and generated in this study are listed in
472 Supplementary Table S2.

473 *DNA cloning*

474 All newly made constructs were verified by sequencing. Constructs expressing
475 candidate ceramide probes were constructed by subcloning the human KSR1 CA3 domain
476 (aa 317-400, XM_047436985), N-terminal C1 domain of human PRKCZ (aa 123-193 ,

477 NM_002744.6), the C-terminal C20 domain of human PRKCZ (aa 405-646), or human SET
478 EMD domain (aa 70-226, NM_001122821.2) into pEGFP-N1 or pmRFP-N1 using restriction
479 sites NheI and XhoI, or into pEGFP-C1 using XhoI and KpnI sites to create C- or N-terminally
480 tagged proteins, respectively. The C-KSR-GS construct replacing the vector-based linker
481 (LELKLRILQS) by a glycine-serine rich linker (GGSSGGGGA) was generated by site directed
482 mutagenesis (Q5 Site-Directed Mutagenesis Kit, NEB, USA) of the C-KSR-EGFP plasmid.
483 The tandem 2x-C-KSR probe was made by subcloning a second CA3 domain together with a
484 flexible linker sequence (GGSSGGGGA) introduced in the primer in between the two CA3
485 domains into C-KSR-EGFP using XhoI and KpnI sites. The sequence encoding the nuclear
486 export signal (NES) from mammalian MAPKK kinase (LQKKLEELEL) was inserted by site
487 directed mutagenesis after the start codons of human PRKCZ C20(405-646) or SET EMD(70-
488 226) to yield plasmids containing C-NES-C20-PRKCZ-EGFP and C-NES-SET-EMD-EGFP,
489 respectively. Two point mutations in the CA3 domain of KSR1 (C359S, C362S) with
490 substitution of the two conserved cysteines with serine residues was introduced using the Q5
491 Site-Directed Mutagenesis Kit. For protein purification from *E.coli,* the KSR1 CA3 domain was
492 cloned into SfiI restriction sites of the pETM11-SUMO3-sfGFP (Saliba et al.) to make pETM11-
493 SUMO3-sfGFP-KSR1. The sequence encoding C-KSR was subcloned into pETM11-SUMO3
494 via Gibson assembly using Gibson Assembly Cloning Kit (NEB, USA). Sequences encoding
495 N-KSR or C-KSR were subcloned into SfiI sites of pSBbi-pur-H-2Kb (# 111623, Addgene,
496 USA) replacing an existing H-2kb fragment. Primers used are listed in Supplementary Table
497 S3.

498 *Cell culture, transfection, and stable cell line establishment*

499 Wild-type mouse embryonic fibroblasts (MEF, ATCC CRL-2991), HeLa cells (ECACC,
500 93021013, a gift from N. Demaurex), and HEK 293T (HEK, ATCC-CRL-11268, a gift from N.
501 Demaurex) were cultured in DMEM (22320, Thermo), MEM (41090, Thermo) and DMEM
502 glutaMAX (31966, Thermo) respectively, containing 10% fetal bovine serum (FBS, Thermo),
503 1% pen/strep (10000 U/ml penicillin, 10 mg/ml streptomycin, PAN Biotech, Germany). JAWS
504 II (JAWS, ATCC CRL-11904) were grown in alpha minimum essential medium with
505 ribonucleosides, deoxyribonucleosides (Gibco 22571), supplemented with 4 mM L-glutamine
506 (Gibco 25030), 1 mM sodium pyruvate (Gibco 58636), 5 ng/ml GM-CSF (Peprotech, 315-03)
507 20% FBS, 1% pen/strep. Delipidated FBS was prepared by incubating FBS with 0.5 g/ml lipid
508 removal beads (13358-U, Sigma/Merck) at 4°C overnight with rotation followed by
509 centrifugation (27,000g, 20 min, 4°C) and supernatant filtration using 0.2 μm PES filters
510 (Nalgene). All cell lines were cultured at 37°C, 5% CO2, and passaged 1-2 times per week,
511 and used between passages 10 and 40. All cell lines were tested every 6-12 months either by
512 PCR (LookOut kit, Sigma/Merck) or Mycostrips (Invivogen, ep-mysnc-50) and were negative.

513 Cells were transfected upon reaching 60-70% confluency 2-3 days after seeding using
514 Lipofectamine 2000 (Thermo) in full culture medium without antibiotics for 4-6h. To prepare
515 DNA-lipofectamine complexes, equal volumes of serum- and antibiotic-free media containing
516 DNA or Lipofectamine were mixed and incubated at room temperature for 1h. To obtain stable
517 cell lines via transposition, MEF cells were first co-transfected with pSBbi-pur plasmids
518 encoding the protein of interest and pCMV-(CAT)T7-SB100 plasmid (#34879, Addgene, USA)
519 encoding Sleeping Beauty transposase SB100x. Puromycin (10 µg/mL) selection was
520 performed 2 days after co-transfection. Stable cell lines (N-KSR and C-KSR) were maintained
521 in full culture medium containing puromycin (10 µg/ml). JAWS transfection was achieved using
522 20 µg DNA and 2 x 10^6 million cells per 100 µl nucleofection solution from the Amaxa
523 Nucleofector Mouse Dendritic Cell kit (Lonza), and the Y-001 program. Cells were diluted in
524 400 µl RPMI 1640 Glutamax medium, 25 mM HEPES medium (Thermo, 72400021)
525 immediately after electroporation, incubated for 10 min at RT, then centrifuged at 200 g, 5 min,
526 RT and resuspended in warm full medium and incubated overnight before imaging.

527 *Immunofluorescence*

528 MEF and HeLa cells seeded on 0.17 mm glass coverslips (Carl Roth) were fixed with
529 4% paraformaldehyde (PFA, AlfaAesar) in PBS for 30 min at RT followed by 3X washes in
530 PBS. JAWS were fixed in 1%PFA for 10 min. For staining nuclei, fixed cells were incubated
531 with 10 µg/ml Hoechst 33342 (Thermo) for 5 min at followed by three washes with PBS and
532 mounting. For immunostainings, cells were permeabilized with 0.1% Triton X-100 (in PBS) for
533 5 min at RT, washed 3X by PBS, quenched with 25 mM Glycine/PBS for 10 min at RT, treated
534 with Image-IT-FX (Thermo) for 30 min followed by blocking with 2% bovine serum albumin
535 (BSA)/PBS for 30 min. After that the cells were incubated with primary antibodies at 4°C
536 overnight and with a secondary antibody for 1h in dark humid chambers, antibodies diluted in
537 blocking buffer. 3x washes in PBS were carried out between each step in the procedure.
538 Finally, the coverslips were mounted onto glass slides using 5 µl of ProLong Diamond
539 Mounting medium (Thermo) per coverslip. For labeling recycling endosomes, MEF cells were
540 incubated for 30 min at 37°C with 50 µg/ml Alexa555-conjugated human transferrin (Thermo)
541 in MEF full culture medium containing 0.2% (BSA). After 2x washed with PBS, cells were fixed
542 with 3% PFA for 20 min, quenched with 50 mM ammonium chloride for 15 min (RT), followed
543 by 3 washes in PBS and mounting. Images were acquired either using Zeiss LSM700 or
544 LSM800 confocal systems /Plan apochromat 63x/1.4 objectives and Zeiss Zen 2010b version
545 service pack1, or Nipkow Okagawa Nikon spinning disk confocal imaging system Plan Apo
546 63x/1.4 DICIII objective and Visiview 4.0 software (Visitron Systems).

547 *Drug treatments*

548 To induce sphingolipid depletion MEF cells were treated with: 0.5 μM myriocin (or
549 methanol vehicle) from *Mycelia sterilia* in full culture medium, with 2.5 μM fumonisin B1
550 (methanol vehicle) from *Fusarium moniliforme* in culture medium containing 10% FBS
551 delipidated as above for 3 days, or with 20 μM fumonisin B1 in regular cell culture medium
552 overnight. To induce sphingolipid production MEF cells were treated with 0.5 mM BSA-
553 conjugated palmitic acid complex (Cayman Chemical, USA) for 4h at 37°C in delipidated-FBS
554 medium, and in regular medium with 100 μM Genz-123346 (DMSO vehicle) overnight, or 200
555 μM C6-ceramide (d18:1/6:0) (Avanti/Merck) for 2h (ethanol vehicle). To induce DAG
556 accumulation cells were treated with 10 μM ionomycin in regular medium for 10 min. To
557 release ceramides locally at the plasma membrane cells were treated with 0.5 U/ml
558 sphingomyelinase from *Staphylococcus aureus* for 30 min in DMEM medium without FBS and
559 antibiotics. After treatment cells were either placed on ice, scraped and used for lipid extraction
560 or fixed with 4% PFA and mounted for microscopy. Alternatively, after SMase treatment, cells
561 were stained with a sphingomyelin probe EGFP-Lysenin (Kiyokawa et al.) (purified from *E.coli,*
562 see below) at 20 μg/ml in serum-free medium for 30 min at 37°C followed by 2 washed in PBS
563 and fixation as described above.

564 *Image analysis*

565 Image analysis was performed using ImageJ v1.52 (Schneider et al.) NIH.
566 Colocalization analysis was conducted using the JACoP v2.0 plugin (Bolte and Cordelières)
567 that returned Mander's coefficients for each region of interest (ROI). Mean fluorescence
568 intensities were measured from background-subtracted images. Analyses determining the
569 percentage of cells displaying plasma membrane localization were conducted on images
570 randomized by the Filename_Randomizer.txt macro
571 https://imagej.nih.gov/ij/macros/Filename_Randomizer.txt, by a blinded experimenter that
572 counted the number of plasma membrane-positive cells and total cells in each image using
573 the Cell Counter plugin. For whole-cell fluorescence intensity analyses, confocal z-stacks of 9
574 frames spaced at 0.5 μm intervals were acquired and sum projections of stacks were created
575 using the Z-Projection tool. Cell and background ROIs were drawn as above on the sum
576 projections images to obtain mean total cellular fluorescence intensities. To eliminate
577 differences between images acquired on LSM700 vs LSM800 microscopes a normalization
578 factor was calculated from images taken on both microscopes from the same coverslip and
579 applied to obtain normalized mean total cellular fluorescence intensities (nMFI).

580 *Immunoblotting*

581 Cells grown to 80-90% confluency on 6-cm dishes were washed 3x with PBS, scraped
582 off, pelleted, and lysed in RIPA buffer (Thermo 89900) with protease inhibitors (Halt Protease

583 Inhibitor cocktail, 87785) for 30 min at 4°C. Cell debris was pelleted at max speed for 10 min
584 (4°C), and the supernatant was used for loading into the gel. Protein concentration was
585 quantitated using RotiQuant kit (Carl Roth). Lysates were diluted in the SDS Loading Buffer
586 (Roti-Load, Carl Roth) and heated at 95°C for 5 min. 15-30 µg protein were loaded and
587 separated by SDS-PAGE in 4–12% SurePAGE 12-well pre-cast gels (Genscript). Proteins
588 were transferred onto PVDF membranes using iBlot or iBlot2 system (Thermo). After transfer,
589 membranes were blocked in 5%milk/TBS-1%Tween-20 (TBST) for 1h (RT, agitation) followed
590 by incubation with primary antibodies diluted in 3%-milk/TBST overnight at 4°C and 1h
591 incubation at RT with HRP-conjugated secondary antibodies 3%-milk/TBST with multiple
592 washes in PBS between incubations with primary and secondary antibodies. Signals were
593 detected using Immobilon HRP substrate (Merck) on the ImageQuant LAS 4000 mini imaging
594 system (GE, USA).

595 *Lipid extraction and lipidomics*

596 For lipidomics experiments, lipids were extracted following a modified MTBE protocol
597 (Guri et al.). MEF cells grown to confluency in lipid-free or full culture medium on 6-cm dishes
598 were washed in cold PBS and scraped off in 1 ml PBS. 900 µl and 100 µl cell suspension were
599 transferred to two separate tubes and the cells were pelleted at 400g for 5 min (4°C). The
600 pellets were kept at -80°C or used for protein quantitation (100 µl sample) by resuspension in
601 RIPA buffer, using RotiQuant as above, or for lipid extraction (900 µl sample) as follows. First,
602 pellets were resuspended in 100 µl LC-MS grade water, then 360 µl methanol and the lipid
603 standard mix (see Reagents section) were added, and the tubes vigorously vortexed. Next,
604 1.2 ml MTBE was added, and the samples were incubated for 1h at RT with shaking. 200 µl
605 of water was added to induce phase separation; samples were incubated at RT for 10 min
606 followed by centrifugation at 1000g, 10 min (RT). The upper organic phase was transferred to
607 13mm glass tube, 400 µl of the artificial upper phase (MTBE/methanol/water (10:3:1.5, v/v))
608 was added, the phase separation was repeated, and the collected second upper phase was
609 combined with the first one. The total lipid extract was divided into 2 equal parts: one for
610 sphingolipids (SL) and one for glycerophospholipids (TL). Extracts were dried in a speed
611 vacuum concentrator. After drying, the samples were flushed with nitrogen unless used for
612 further steps. The sphingolipid aliquot was treated with methylamine to remove phospholipids
613 by de-acylation (Clarke method (Clarke and Dawson)). 0.5 mL monomethylamine reagent
614 (MeOH/H2O/n-butanol/Methylamine solution (4:3:1:5 v/v) was added to the dried lipids, tubes
615 sonicated for 6 min, vortexed, followed by the incubation for 1h at 53°C. Finally, the
616 methylamine-treated fraction was dried (as mentioned above). The monomethylamine-treated
617 lipids were subjected to desalting via extraction with *n*-butanol. In short, 300 µl water-saturated
618 *n*-butanol (*n*-butanol/water 2:1 v/v, mixed and prepared at least 1 day before use) was added

619 to the dried lipids. The samples were vortexed and sonicated for 6 min, and 150 µl LC-MS
620 grade water was added. The mixture was vortexed thoroughly and centrifuged at 3200 x g for
621 10 min. The upper phase was transferred to a 2 mL amber vial. The lower phase extraction
622 was repeated as described above twice more, and the organic phases were combined and
623 dried.

624 Targeted lipidomic analysis by mass spectrometry was performed according to prior
625 protocols (Jiménez-Rojo et al.) as follows: TL and SL aliquots were resuspended either in 250
626 µl Chloroform: Methanol (LC-MS grade, 1:1 v/v) or directly in the sample solvent
627 ((chloroform/methanol/water (2:7:1 v/v) + 5mM ammonium acetate). After sonication for 6 min
628 (RT), lipid mixtures were transferred into wells of a 96-well Twin tech PCR plate (Eppendorf)
629 using Hamilton syringes. Sphingolipid aliquots were diluted 1:4, and total lipids were diluted
630 1:10 in the sample solvent. PCR plate was sealed with EasyPierce foil (Thermo), and the
631 samples were injected into the TSQ Vantage Triple Stage Quadrupole mass spectrometer
632 (Thermo Fisher Scientific) equipped with a robotic sample handler and nanoflow ion source
633 Nanomate HD (Advion Biosciences, USA). The collision energy was optimized for each lipid
634 class. Lipid detection parameters are listed in Supplementary Table S4. Samples were
635 injected at a gas pressure of 30 psi with a spray voltage of 1.2 kV and run on the mass
636 spectrometer operated with a spray voltage of 3.5 kV for positive mode and 3.0 kV for negative
637 mode and a capillary temperature set at 190oC. Sphingolipid and glycerophospholipid species
638 were identified and quantified using multiple reaction monitoring (MRM). Ceramide species
639 were also quantified with a loss of water in the first quadrupole. Each biological replicate was
640 measured twice (2 technical replicates, TR). Each TR consisted of 3 measurements for each
641 transition. Each lipid species was quantified using standard curves created from internal
642 standards. Data analysis was performed using R version 3.6.2 (R Foundation for Statistical
643 Computing). The values where then normalized to the total lipid content of each corresponding
644 lipid extract (mol% of the sum of total PC, PE, PI, PS), except for samples of phagocytosing
645 cells. In this case, because large changes in PC under the phagocytosing condition skewed
646 the normalization, lipid concentrations were normalized first to total protein of each
647 corresponding individual sample, then to the average of the sum of total PC, PE, PI, PS for
648 the entire sample group (control and phagocytosing) processed the same day. Lipid values
649 are thus expressed as mol% of the daily average total lipid mass (mol% of ave tot). Values
650 greater than 100% thus represent values greater than the average total lipid.

651 *Protein purification from E.coli*

652 Rosetta 2(DE3) *E.coli* cells (Novagen) were transformed with the plasmids expressing
653 His6-SUMO3 tagged KSR probes or GFP alone (control): pETM11-His6-SUMO3- -sfGFP-N-

654 KSR, pETM11-His6-SUMO3-C-KSR-sfGFP, pETM11-His6-SUMO3-sfGFP. Transformed
655 bacteria were grown at 37°C in 1L LB medium containing 100 µg/ml kanamycin, 34 µg/ml
656 chloramphenicol until OD600 0.6-0.8. Protein expression was induced by the overnight
657 incubation with 0.4 mM isopropyl β-D-thiogalactoside (IPTG) at 16°C. The next day bacteria
658 were lysed using the Microfluidizer LM20 high-pressure homogenizer (15,000 psi pressure, 2
659 cycles) in lysis buffer (50 mM Tris pH 7.5, 500 mM NaCl, 20 mM imidazole, protease inhibitors
660 (1 tablet/50 mL), 0.5 mM DTT) and the soluble fraction was obtained by centrifugation at
661 16,000g for 1h (4°C). Proteins harboring the His6 tag were captured by incubation with Ni-
662 NTA resin (Qiagen) (2ml resin per bacterial lysate from 1L culture) for 2h, 4°C, 30 rpm rotation.
663 Agarose resin with bound proteins was centrifuged at 1200 rpm, 8 min (4°C), and the slurry
664 was transferred to a column with a cotton filter. The column was washed with 20 ml Lysis
665 buffer, His6-tagged proteins were eluted with 6 ml Elution Buffer (50 mM Tris pH 7.5, 250 mM
666 NaCl, 500 mM imidazole), DTT was added to 5 mM to prevent protein aggregation. Eluted
667 proteins were dialyzed against 50 mM Tris pH 7.5, 200 mM NaCl, 1 mM DTT overnight at 4°C.
668 The His6-SUMO3 tag was cleaved off the proteins by incubation with His-tagged SenP2
669 protease (EMBL Protein Expression and Purification Core Facility European, Germany) at a
670 molar ratio of SenP2 to protein 40:1. The undigested proteins and the protease were removed
671 using Ni-NTA resin, purified proteins were eluted by applying Elution Buffer 2 (50 mM Tris pH
672 7.5, 250 mM NaCl, 10 mM imidazole) to Ni-NTA-packed column. The quality of purification
673 was assessed by SDS-PAGE followed by Coomassie staining (RotiBlue kit, CarlRoth). sfGFP-
674 N-KSR was further purified by size exclusion chromatography on the S75 column pre-
675 equilibrated with 50 mM mM Tris, pH 7.4 and 250 mM NaCl.

676 *Cell lysate preparation from HEK cells*

677 HEK cells grown on 10-cm dishes in HEK full culture medium to 70-80% confluency
678 were transfected as above with plasmids encoding EGFP (control), KSR lipid probes, or PKC-
679 C1(2)-GFP, where 20 µg plasmid DNA/50 µl lipofectamine 2000 was used per dish. After
680 overnight incubation, the cells were trypsinized for 1 min (RT) and resuspended in PBS
681 containing 0.5 mM EDTA. Cells suspension was centrifuged 200g, 5 min (4°C), followed by a
682 wash in PBS. After pelleting, cells were resuspended in 120 µl hypotonic lysis buffer (10 mM
683 Tris-HCl, pH=7.5, Halt protease and phosphatase inhibitors) and incubated on ice for 20 min.
684 Cells were lysed by passing the suspension 15 times through a 30G syringe needle. Protein
685 concentration was measured using a NanoDrop (Thermo). Finally, NaCl and DTT were added
686 to 150 mM and 5 mM, respectively.

687 *Liposome Microarray-based assay (LiMA)*

688 Liposome-based protein-lipid interaction assay was performed following the protocol
689 described in (Saliba et al.). Lipid mixtures of different compositions were prepared in
690 chloroform: methanol: water (20:9:1 v/v/v). DOPC-based liposomes contained: 0.1 mol %
691 fluorescent lipid PE-Atto647, 0.5% mol stabilizing lipid PE-PEG350, and 2%, 5% or 10% of
692 bovine ceramide mixture (CerMix), C18-ceramide (C18Cer), C18-dihydroceramide (DHCer),
693 sphingomyelin (SM), glucosyl-ceramide (GlcCer), sphingosine (Sph), sphingosine-1-
694 phosphate (S1P), ceramide-1-phosphate (Cer1P), diacylglycerol (DAG), or 10%
695 phosphatidylinositol-4,5-bisphosphate (PI(4,5)P2) (see also Supplementary Table S1). IPM
696 mimicking liposomes were based on a POPC carrier lipid backbone with 0.1 mol % fluorescent
697 lipid PE-Atto647, 0.5% mol stabilizing lipid PE-PEG350, 33% cholesterol, 21.2% DOPS,
698 15%POPE, and 2%, 5%, or 10% CerMix, C18DHCer, C18Cer, DAG, POPA, SM and Sph.
699 Mixtures containing 5% and 10% GlcCer or 10% DAG did not form liposome, and all liposomes
700 containing DOPA were autofluorescent, thus these spots were excluded from the analysis.
701 Lipids were spotted onto thin agarose layers covered by the protective membrane on top of a
702 glass slide using automated lipid spotting under an inert argon atmosphere (Automatic TLC-
703 spotter4, Camag, Switzerland). A microfluidic chamber with four channels was manufactured
704 from polydimethylsiloxane (PDMS), as described in (Saliba et al.). Then the agarose layers
705 with spotted lipids were glued onto PDMS chambers using a 2:1 mixture of silicone elastomer:
706 curing agent diluted 3× (v/v) in hexane as an adhesive, so the resulting microfluidic chamber
707 contained four channels of 30 spots, 120 lipid spots per chamber. Liposomes were generated
708 by manually injecting the liposome buffer (10 mM HEPES, 150 mM NaCl) into each channel
709 with a Hamilton syringe. Then, 40 µl of the solution containing purified proteins at 5-10 µM or
710 HEK cell lysates in liposome buffer with 5 mM DTT were injected into channels using an
711 automated injection system with a flow rate of 8 µl/min. After incubation of freshly formed
712 liposomes with the GFP-tagged proteins for 1h at RT, the channels were manually washed
713 with 80 µl of liposome buffer, and all spots in the chamber were imaged with a Zeiss Axio
714 Observer Z1 video time-lapse system. All images were taken with the 20x objective; liposomes
715 were imaged with the Cy5 filter set (5 and 10 ms exposure), and GFP-tagged proteins were
716 imaged at different exposure times (1, 5, 10, 25, 50, 75, 100, 150, 200, and 300 ms).

717 Images were analyzed using CellProfiler version 4.2.5 software (Broad Institute) using
718 a custom pipeline described in detail in (Saliba et al.). A custom-made R script was used to
719 calculate the normalized binding intensity value (NBI) for each protein-lipid interaction. NBI
720 represents a mean of the ratio of GFP to Atto647 fluorescence divided by exposure time at all
721 exposure times for which spots were successfully segmented and is proportional to the
722 amount of GFP-tagged interaction protein recruited to the liposome surface. NBI scores were

723 then expressed as the Log2 ratio of liposome of interest to control liposome containing carrier,
724 fluorescent and stabilizer lipids only.

725 *Preparation of phagocytic beads and phagocytosis*

726 3 µm carboxyl polystyrene beads (Spherotech, CP30-10) were covalently coupled with
727 purified human IgG (hIgG, Dunn Labortechnik, Germany) by washing 3 times in sterile PBS
728 with centrifugation at maximum speed (18,000 g) at 4°C, activating with 50 mM 1-ethyl-3-(3-
729 dimethylaminopropyl) carbodiimide hydrochloride (EDC-HCl, Carl Roth/2156.1) for 15 min in
730 PBS at room temperature (RT) with rigorous shaking, followed by 3 washes at 4°C in 0.1 M
731 Na2B4O7 buffer (pH 8.0). Finally, 2 µg/µl of hIgG (and 15 ng/µl iFluor647-amine (AAT
732 Bioquest), for fluorescent beads) were added to the beads and incubated overnight at 4°C on
733 a shaker. The next day, the beads were washed 2x with 250 mM glycine/PBS followed by two
734 washes in PBS. To render MEFs phagocytic, cells were transfected with 1 µg/2x10^5 cells
735 pcDNA3-myc-FCGR2A (Fc receptor) plus KSR1-based probes and where indicated TagRFP-
736 KDEL, mCherry-STIM1 or mCherry-Sec22b at 0.3 µg per 2x10^5 cells. Cells were washed in
737 full medium 4-6h after transfection. The following day beads were added to the cells at a bead-
738 to-cell ratio 10:1, cells were centrifuged at 200g, 2 min, RT, incubated with the beads for the
739 indicated times at 37°C, washed with PBS, fixed with 4% PFA/PBS for 30 min followed by 3x
740 washes with PBS and mounting as described above.

741

742 **Statistics and reproducibility**

743

744 All statistical analyses were done using Prism (GraphPad Software). P values that are
745 significant are shown above the bars. Two-tailed unpaired t-test were performed when
746 comparing two samples, Welch's correction was used if F test showed a significant difference
747 in variance. For three or more sample comparisons a one-way ANOVA was employed with in
748 case of negative F test, and Brown-Forsythe and Welch test in case F test showed significant
749 difference in variance, with Dunnett's post-hoc test. For lipidomic data multiple ratio paired t-
750 test was performed with a two-stage step-up method (Benjamini, Krieger, and Yekutieli), with
751 a false discovery rate set at 5%. Categorical quantification of plasma membrane recruitment
752 was performed by a blinded experimenter on randomized images. Contingency tables were
753 analysed using a Chi-squared test. Cells exhibiting abnormal morphology (multinucleated,
754 high vacuolation) or signs of death (blebbing) were excluded from analysis. A minimum of 5
755 replicate fields per coverslip are imaged for analysis of fixed cells. These may contain from 1
756 to tens of cells or 1 to tens of phagosomes which are considered as replicate values. For
757 liposome analysis spots with large aggregrates were excluded from the analysis.

758

759 **Data availability**

760 Full datasets, including all microscopy and Western blot source images will be made
761 available on the University of Geneva's FAIR-compliant data repository Yareta under a CC BY
762 4.0 licence upon publication. Plasmids generated in this study will be deposited on Addgene
763 upon publication, to be distributed subject to a standard Material's Transfer Agreement.

764

765 **Acknowledgements**

766 We are grateful to the bioimaging and proteins and peptides core facilities at the
767 University of Geneva Medical Centre, Faculty of Medicine as well as the mass spectrometry
768 core facility at the Faculty of Science for their invaluable help. Thanks to Drs. Nicolas
769 Demaurex, Maud Frieden, Brenda Kwak and Amado Carreras-Sureda for their valuable
770 advice. This work was funded by a Professor Dr. Max Cloëtta Foundation Medical Researcher
771 Grant (to PNH), a Swiss National Science Foundation grant (310030_189094, to PNH), a
772 Schmidheiney Foundation subsidy (2022) to PNH. HR acknowledges the Swiss National
773 Science Foundation (310030_184949), the NCCR Chemical Biology (51NF40-185898) and
774 the Leducq Foundation. ACG and LVE acknowledge the financial support of the Louis-Jeantet
775 Foundation, Switzerland.

776

777 **Author Contributions**

778 VG designed and performed experiments, analysed data and wrote the manuscript.
779 LVE, IDQ, MA and MCC designed and performed experiments and analysed data. IR, and
780 MM performed experiments and analysed data. HR and ACG designed experiments, provided
781 guidance on analysis and interpretation of data as well as materials. PNH conceived the
782 project, designed and performed experiments and wrote the manuscript.

783

784 **Competing Interests**

785 The authors declare no competing interests.

786 **References**

787 **Abe, M. and Kobayashi, T.** (2014). Imaging local sphingomyelin-rich domains in the plasma
788 membrane using specific probes and advanced microscopy. *Biochim Biophys Acta* **1841**, 720-6.

Adachi, Y., Pavlakis, G. N. and Copeland, T. D. (1994). Identification and characterization of SET, a nuclear phosphoprotein encoded by the translocation break point in acute undifferentiated leukemia. *Journal of Biological Chemistry* **269**, 2258-2262.

Albi, E. and Viola Magni, M. P. (1997). Chromatin neutral sphingomyelinase and its role in hepatic regeneration. *Biochemical and Biophysical Research Communications* **236**, 29-33.

Avota, E., Gulbins, E. and Schneider-Schaulies, S. (2011). DC-SIGN mediated sphingomyelinase-activation and ceramide generation is essential for enhancement of viral uptake in dendritic cells. *PLoS Pathog* **7**, e1001290.

Bakr, A., Shakor, A., Kwiatkowska, K. and Sobota, A. (2004). Cell Surface Ceramide Generation Precedes and Controls Fc RII Clustering and Phosphorylation in Rafts*. *Journal of Biological Chemistry* **279**, 36778--36787 , pmid = 15194692.

Bakrac, B., Kladnik, A., Macek, P., McHaffie, G., Werner, A., Lakey, J. H. and Anderluh, G. (2010). A toxin-based probe reveals cytoplasmic exposure of Golgi sphingomyelin. *J Biol Chem* **285**, 22186-95.

Bidlingmaier, S., Ha, K., Lee, N. K., Su, Y. and Liu, B. (2016). Proteome-wide Identification of Novel Ceramide-binding Proteins by Yeast Surface cDNA Display and Deep Sequencing. *Mol Cell Proteomics* **15**, 1232-45.

Bjørnestad, V. A. and Lund, R. (2023). Pathways of Membrane Solubilization: A Structural Study of Model Lipid Vesicles Exposed to Classical Detergents. *Langmuir* **39**, 3914-3933.

Bockelmann, S., Mina, J. G. M., Korneev, S., Hassan, D. G., Muller, D., Hilderink, A., Vlieg, H. C., Raijmakers, R., Heck, A. J. R., Haberkant, P. et al. (2018). A search for ceramide binding proteins using bifunctional lipid analogs yields CERT-related protein StarD7. *J Lipid Res* **59**, 515-530.

Bodman-Smith, K. B., Gregory, R. E., Harrison, P. T. and Raynes, J. G. (2004). FcγRIIa expression with FcγRI results in C-reactive protein- and IgG-mediated phagocytosis. *Journal of Leukocyte Biology* **75**, 1029-1035.

Bolte, S. and Cordelières, F. P. (2006). A guided tour into subcellular colocalization analysis in light microscopy. *J Microsc* **224**, 213-32.

Botelho, R. J., Teruel, M., Dierckman, R., Anderson, R., Wells, A., York, J. D., Meyer, T. and Grinstein, S. (2000). Localized biphasic changes in phosphatidylinositol-4,5-bisphosphate at sites of phagocytosis. *J Cell Biol* **151**, 1353-68.

Brennan, J. A., Volle, D. J., Chaika, O. V. and Lewis, R. E. (2002). Phosphorylation regulates the nucleocytoplasmic distribution of kinase suppressor of Ras. *Journal of Biological Chemistry* **277**, 5369-5377.

Buchberger, A. R., DeLaney, K., Johnson, J. and Li, L. (2018). Mass Spectrometry Imaging: A Review of Emerging Advancements and Future Insights. *Anal Chem* **90**, 240-265.

Canals, D., Salamone, S. and Hannun, Y. A. (2018). Visualizing bioactive ceramides. *Chem Phys Lipids* **216**, 142-151.

Canton, J., Blees, H., Henry, C. M., Buck, M. D., Schulz, O., Rogers, N. C., Childs, E., Zelenay, S., Rhys, H., Domart, M.-C. et al. (2021). The receptor DNGR-1 signals for phagosomal rupture to promote cross-presentation of dead-cell-associated antigens. *Nature Immunology* **22**, 140-153.

Childs, E., Henry, C. M., Canton, J. and Reis e Sousa, C. (2021). Maintenance and loss of endocytic organelle integrity: mechanisms and implications for antigen cross-presentation. *Open Biol* **11**, 210194.

Clarke, N. G. and Dawson, R. M. (1981). Alkaline O leads to N-transacylation. A new method for the quantitative deacylation of phospholipids. *Biochemical Journal* **195**, 301-301.

Codazzi, F., Teruel, M. N. and Meyer, T. (2001). Control of astrocyte Ca(2+) oscillations and waves by oscillating translocation and activation of protein kinase C. *Curr Biol* **11**, 1089-97.

Contreras, F. X., Basañez, G., Alonso, A., Herrmann, A. and Goñi, F. M. (2005). Asymmetric Addition of Ceramides but not Dihydroceramides Promotes Transbilayer (Flip-Flop) Lipid Motion in Membranes. *Biophysical Journal* **88**, 348-359.

Contreras, F. X., Villar, A. V., Alonso, A. and Goñi, F. M. (2009). Ceramide-induced transbilayer (flip-flop) lipid movement in membranes. *Methods Mol Biol* **462**, 155-65.

Criado Santos, N., Bouvet, S., Cruz Cobo, M., Mandavit, M., Bermont, F., Castelbou, C., Mansour, F., Azam, M., Giordano, F. and Nunes-Hasler, P. (2023). Sec22b regulates phagosome maturation by promoting ORP8-mediated lipid exchange at endoplasmic reticulum-phagosome contact sites. *Commun Biol* **6**, 1008.

Deng, Y., You, L., Lu, Y., Han, S., Wang, J., Vicas, N., Chen, C. and Ye, J. (2021). Identification of TRAMs as sphingolipid-binding proteins using a photoactivatable and clickable short-chain ceramide analog. *J Biol Chem* **297**, 101415.

Devaux, P. F. (1991). Static and Dynamic Lipid Asymmetry in Cell Membranes. *Biochemistry* **30**, 1163-1173.

Duran, J. M., Campelo, F., van Galen, J., Sachsenheimer, T., Sot, J., Egorov, M. V., Rentero, C., Enrich, C., Polishchuk, R. S., Goni, F. M. et al. (2012). Sphingomyelin organization is required for vesicle biogenesis at the Golgi complex. *EMBO J* **31**, 4535-46.

Ekman, P., Maula, T., Yamaguchi, S., Yamamoto, T., Nyholm, T. K. M., Katsumura, S. and Slotte, J. P. (2015). Formation of an ordered phase by ceramides and diacylglycerols in a fluid phosphatidylcholine bilayer — Correlation with structure and hydrogen bonding capacity. *Biochimica et Biophysica Acta (BBA) - Biomembranes* **1848**, 2111-2117.

Freeman, S. A. and Grinstein, S. (2014). Phagocytosis: receptors, signal integration, and the cytoskeleton. *Immunol Rev* **262**, 193-215.

Fuglsang, E., Boye, L. and Frøkiær, H. (2017). Enhancement of ceramide formation increases endocytosis of Lactobacillus acidophilus and leads to increased IFN-β and IL-12 production in dendritic cells. *J. Clin. Immunol. Res* **1**, 1-9.

Gallegos, L. L., Kunkel, M. T. and Newton, A. C. (2006). Targeting protein kinase C activity reporter to discrete intracellular regions reveals spatiotemporal differences in agonist-dependent signaling. *J Biol Chem* **281**, 30947-30956.

Giodini, A., Rahner, C. and Cresswell, P. (2009). Receptor-mediated phagocytosis elicits cross-presentation in nonprofessional antigen-presenting cells. *Proceedings of the National Academy of Sciences* **106**, 3324-3329.

Goñi, F. M. and Alonso, A. (1999). Structure and functional properties of diacylglycerols in membranes. *Progress in Lipid Research* **38**, 1-48.

Goñi, F. M., Contreras, F. X., Montes, L. R., Sot, J. and Alonso, A. (2005). Biophysics (and sociology) of ceramides. *Biochemical Society symposium*, 177-188.

Götz, R., Kunz, T. C., Fink, J., Solger, F., Schlegel, J., Seibel, J., Kozjak-Pavlovic, V., Rudel, T. and Sauer, M. (2020). Nanoscale imaging of bacterial infections by sphingolipid expansion microscopy. *Nature Communications 2020 11:1* **11**, 1-9.

Goulden, B. D., Pacheco, J., Dull, A., Zewe, J. P., Deiters, A. and Hammond, G. R. V. (2019). A high-avidity biosensor reveals plasma membrane PI(3,4)P2 is predominantly a class I PI3K signaling product. *Journal of Cell Biology* **218**, 1066-1079.

Guido, D., Demaurex, N. and Nunes, P. (2015). Junctate boosts phagocytosis by recruiting endoplasmic reticulum Ca2+ stores near phagosomes. *J Cell Sci* **128**, 4074-82.

Guri, Y., Colombi, M., Dazert, E., Hindupur, S. K., Roszik, J., Moes, S., Jenoe, P., Heim, M. H., Riezman, I., Riezman, H. et al. (2017). mTORC2 Promotes Tumorigenesis via Lipid Synthesis. *Cancer Cell* **32**, 807-823.e12.

Hammond, G. R. V., Ricci, M. M. C., Weckerly, C. C. and Wills, R. C. (2022). An update on genetically encoded lipid biosensors. *Mol Biol Cell* **33**.

Hannun, Y. A. and Obeid, L. M. (2008). Principles of bioactive lipid signalling: Lessons from sphingolipids, vol. 9, pp. 139--150 , pmid = 18216770.

Hannun, Y. A. and Obeid, L. M. (2018). Sphingolipids and their metabolism in physiology and disease, vol. 19, pp. 175--191 , pmid = 29165427: Nature Publishing Group.

Hinkovska-Galcheva, V., Boxer, L. A., Kindzelskii, A., Hiraoka, M., Abe, A., Goparju, S., Spiegel, S., Petty, H. R. and Shayman, J. A. (2005). Ceramide 1-Phosphate, a Mediator of Phagocytosis*.

Jiménez-Rojo, N., Leonetti, M. D., Zoni, V., Colom, A., Feng, S., Iyengar, N. R., Matile, S., Roux, A., Vanni, S., Weissman, J. S. et al. (2020). Conserved Functions of Ether Lipids and Sphingolipids in the Early Secretory Pathway. *Curr Biol* **30**, 3775-3787.e7.

Kiefer, K., Carreras-Sureda, A., García-López, R., Rubio-Moscardó, F., Casas, J., Fabriàs, G. and Vicente, R. (2015). Coordinated regulation of the orosomucoid-like gene family expression controls de novo ceramide synthesis in mammalian cells. *J Biol Chem* **290**, 2822-30.

Kiyokawa, E., Baba, T., Otsuka, N., Makino, A., Ohno, S. and Kobayashi, T. (2005). Spatial and Functional Heterogeneity of Sphingolipid-rich Membrane Domains. *Journal of Biological Chemistry* **280**, 24072-24084.

Kjellberg, M. A., Lönnfors, M., Slotte, J. P. and Mattjus, P. (2015). Metabolic conversion of ceramides in HeLa cells - A cholesteryl phosphocholine delivery approach. *PLoS One* **10**, 1-19.

Koike, K., Berdyshev, E. V., Mikosz, A. M., Bronova, I. A., Bronoff, A. S., Jung, J. P., Beatman, E. L., Ni, K., Cao, D., Scruggs, A. K. et al. (2019). Role of Glucosylceramide in Lung Endothelial Cell Fate and Emphysema. *Am J Respir Crit Care Med* **200**, 1113-1125.

Krishnamurthy, K., Dasgupta, S. and Bieberich, E. (2007). Development and characterization of a novel anti-ceramide antibody. *Journal of Lipid Research* **48**, 968-975.

Kwiatkowska, K., Hordejuk, R., Szymczyk, P., Kulma, M., Abdel-Shakor, A.-B., Płucienniczak, A., Dołowy, K., Szewczyk, A. and Sobota, A. (2007). Lysenin-His, a sphingomyelin-recognizing toxin, requires tryptophan 20 for cation-selective channel assembly but not for membrane binding. *Molecular Membrane Biology* **24**, 121-134.

Ledeen, R. W. and Wu, G. (2008). Nuclear sphingolipids: metabolism and signaling. *J Lipid Res* **49**, 1176-86.

Levin, R., Grinstein, S. and Canton, J. (2016). The life cycle of phagosomes: formation, maturation, and resolution. *Immunol Rev* **273**, 156-79.

Lorent, J. H., Levental, K. R., Ganesan, L., Rivera-Longsworth, G., Sezgin, E., Doktorova, M., Lyman, E. and Levental, I. (2020). Plasma membranes are asymmetric in lipid unsaturation, packing and protein shape. *Nature Chemical Biology* **16**, 644-652.

Magenau, A., Benzing, C., Proschogo, N., Don, A. S., Hejazi, L., Karunakaran, D., Jessup, W. and Gaus, K. (2011). Phagocytosis of IgG-coated polystyrene beads by macrophages induces and requires high membrane order. *Traffic* **12**, 1730-43.

Majeski, A. E. and Fred Dice, J. (2004). Mechanisms of chaperone-mediated autophagy. *The International Journal of Biochemistry & Cell Biology* **36**, 2435-2444.

Matheny, S. A., Chen, C., Kortum, R. L., Razidlo, G. L., Lewis, R. E. and White, M. A. (2004). Ras regulates assembly of mitogenic signalling complexes through the effector protein IMP. *Nature* **427**, 256-260.

Mathias, S., Peña, L. A. and Kolesnick, R. N. (1998). Signal transduction of stress via ceramide. *Biochemical Journal* **335**, 465-480.

Merrill, A. H., Jr., Sullards, M. C., Wang, E., Voss, K. A. and Riley, R. T. (2001). Sphingolipid metabolism: roles in signal transduction and disruption by fumonisins. *Environ Health Perspect* **109 Suppl 2**, 283-9.

Miyake, Y., Kozutsumi, Y., Nakamura, S., Fujita, T. and Kawasaki, T. (1995). Serine Palmitoyltransferase Is the Primary Target of a Sphingosine-like Immunosuppressant, ISP-1/Myriocin. *Biochemical and Biophysical Research Communications* **211**, 396-403.

Mukhopadhyay, A., Saddoughi, S. A., Song, P., Sultan, I., Ponnusamy, S., Senkal, C. E., Snook, C. F., Arnold, H. K., Sears, R. C., Hannun, Y. A. et al. (2009). Direct interaction between the inhibitor 2 and ceramide via sphingolipid-protein binding is involved in the regulation of protein phosphatase 2A activity and signaling. *FASEB J* **23**, 751-63.

Niekamp, P., Guzman, G., Leier, H. C., Rashidfarrokhi, A., Richina, V., Pott, F., Barisch, C., Holthuis, J. C. M. and Tafesse, F. G. (2021). Sphingomyelin Biosynthesis Is Essential for Phagocytic Signaling during \textless i \textgreater Mycobacterium tuberculosis \textless /i \textgreater Host Cell Entry. *mBio* **12**.

Niekamp, P., Scharte, F., Sokoya, T., Vittadello, L., Kim, Y., Deng, Y., Südhoff, E., Hilderink, A., Imlau, M., Clarke, C. J. et al. (2022). Ca2+-activated sphingomyelin scrambling and turnover mediate ESCRT-independent lysosomal repair. *Nature Communications* **13**, 1875.

Nunes-Hasler, P., Maschalidi, S., Lippens, C., Castelbou, C., Bouvet, S., Guido, D., Bermont, F., Bassoy, E. Y., Page, N., Merkler, D. et al. (2017). STIM1 promotes migration, phagosomal maturation and antigen cross-presentation in dendritic cells. *Nat Commun* **8**, 1852.

Nunes, P., Cornut, D., Bochet, V., Hasler, U., Oh-Hora, M., Waldburger, J. M. and Demaurex, N. (2012). STIM1 juxtaposes ER to phagosomes, generating Ca(2)(+) hotspots that boost phagocytosis. *Curr Biol* **22**, 1990-7.

Pathak, D., Mehendale, N., Singh, S., Mallik, R. and Kamat, S. S. (2018). Lipidomics Suggests a New Role for Ceramide Synthase in Phagocytosis. *ACS Chem Biol* **13**, 2280-2287.

Pédelacq, J. D., Cabantous, S., Tran, T., Terwilliger, T. C. and Waldo, G. S. (2006). Engineering and characterization of a superfolder green fluorescent protein. *Nature Biotechnology* **24**, 79-88.

Pérez-rivas, L. G., Prieto, S. and Lozano, J. (2010). 1 . Modulation of Ras signaling by the KSR family of molecular scaffolds. *Emerging Signaling Pathways in Tumor Biology* **661**, 1-23.

Pohl, A., López-Montero, I., Rouvière, F., Giusti, F. and Devaux, P. F. (2009). Rapid transmembrane diffusion of ceramide and dihydroceramide spin-labelled analogues in the liquid ordered phase. *http://dx.doi.org/10.1080/09687680902733815* **26**, 194-204.

Quinville, B. M., Deschenes, N. M., Ryckman, A. E., Walia, J. S., Ryckman, N. M. and Walia, A. E. (2021). Molecular Sciences A Comprehensive Review: Sphingolipid Metabolism and Implications of Disruption in Sphingolipid Homeostasis.

Razidlo, G. L., Kortum, R. L., Haferbier, J. L. and Lewis, R. E. (2004). Phosphorylation regulates KSR1 stability, ERK activation, and cell proliferation. *Journal of Biological Chemistry* **279**, 47808-47814.

Rinaldi, L., Delle Donne, R., Sepe, M., Porpora, M., Garbi, C., Chiuso, F., Gallo, A., Parisi, S., Russo, L., Bachmann, V. et al. (2016). praja2 regulates KSR1 stability and mitogenic signaling. *Cell Death & Disease* **7**, e2230-e2230.

Saharan, O., Mehendale, N. and Kamat, S. S. (2022). Phagocytosis: A (Sphingo)Lipid Story. *Current Research in Chemical Biology* **2**, 100030.

Saliba, A.-E., Vonkova, I., Ceschia, S., Findlay, G. M., Maeda, K., Tischer, C., Deghou, S., Van Noort, V., Bork, P., Pawson, T. et al. (2014). A quantitative liposome microarray to systematically characterize protein-lipid interactions. *Nature Methods* **11**, 47-50.

Sallusto, F. and Nicol. (1996). Ceramide inhibits antigen uptake and presentation by dendritic cells. *Journal of Experimental Medicine* **184**, 2411--2416 , pmid = 8976196.

Schneider, C. A., Rasband, W. S. and Eliceiri, K. W. (2012). NIH Image to ImageJ: 25 years of image analysis. *Nature Methods* **9**, 671-675.

Schramm, M., Herz, J., Haas, A., Krönke, M. and Utermöhlen, O. (2008). Acid sphingomyelinase is required for efficient phago-lysosomal fusion. *Cell Microbiol* **10**, 1839-53.

Scorrano, L., De Matteis, M. A., Emr, S., Giordano, F., Hajnoczky, G., Kornmann, B., Lackner, L. L., Levine, T. P., Pellegrini, L., Reinisch, K. et al. (2019). Coming together to define membrane contact sites. *Nat Commun* **10**, 1287.

Stewart, S., Sundaram, M., Zhang, Y., Lee, J., Han, M. and Guan, K.-L. (1999). Kinase Suppressor of Ras Forms a Multiprotein Signaling Complex and Modulates MEK Localization. *Molecular and Cellular Biology* **19**, 5523-5534.

988 **Suzuki, J., Fujii, T., Imao, T., Ishihara, K., Kuba, H. and Nagata, S.** (2013). Calcium-dependent
989 phospholipid scramblase activity of TMEM16 protein family members. *J Biol Chem* **288**, 13305-
990 13316.
991 **Tafesse, F. G., Rashidfarrokhi, A., Schmidt, F. I., Freinkman, E., Dougan, S., Dougan, M.,**
992 **Esteban, A., Maruyama, T., Strijbis, K. and Ploegh, H. L.** (2015). Disruption of Sphingolipid
993 Biosynthesis Blocks Phagocytosis of Candida albicans. *PLoS Pathogens* **11**, e1005188 , pmid =
994 26431038.
995 **Tang, J. C. Y., Drokhlyansky, E., Etemad, B., Rudolph, S., Guo, B., Wang, S., Ellis, E. G., Li, J.**
996 **Z. and Cepko, C. L.** (2016). Detection and manipulation of live antigen-expressing cells using
997 conditionally stable nanobodies. *Elife* **5**, e15312-e15312.
998 **Tran, T. T. T., Postal, B. G., Demignot, S., Ribeiro, A., Osinski, C., De Barros, J. P. P.,**
999 **Blachnio-Zabielska, A., Leturque, A., Rousset, M., Ferré, P. et al.** (2016). Short Term Palmitate
1000 Supply Impairs Intestinal Insulin Signaling via Ceramide Production. *J Biol Chem* **291**, 16328-16328.
1001 **Vieu, C., Tercé, F., Chevy, F., Rolland, C., Barbaras, R., Chap, H., Wolf, C., Perret, B. and**
1002 **Collet, X.** (2002). Coupled assay of sphingomyelin and ceramide molecular species by gas liquid
1003 chromatography. *Journal of Lipid Research* **43**, 510-522.
1004 **Walter, T., Schlegel, J., Burgert, A., Kurz, A., Seibel, J. and Sauer, M.** (2017). Incorporation
1005 studies of clickable ceramides in Jurkat cell plasma membranes. *Chemical Communications* **53**, 6836-
1006 6839.
1007 **Wang, G., Krishnamurthy, K., Umapathy, N. S., Verin, A. D. and Bieberich, E.** (2009). The
1008 carboxyl-terminal domain of atypical protein kinase Czeta binds to ceramide and regulates junction
1009 formation in epithelial cells. *J Biol Chem* **284**, 14469-75.
1010 **Wang, G., Silva, J., Krishnamurthy, K., Tran, E., Condie, B. G. and Bieberich, E.** (2005). Direct
1011 binding to ceramide activates protein kinase Czeta before the formation of a pro-apoptotic complex
1012 with PAR-4 in differentiating stem cells. *J Biol Chem* **280**, 26415-26424.
1013 **Williamson, P.** (2015). Phospholipid Scramblases. *Lipid Insights* **8**, 41-44.
1014 **Wu, Y., Li, C., Riehle, A., Pollmeier, B., Gulbins, E. and Grassme, H.** (2018). Mycobacterial
1015 Infection is Promoted by Neutral Sphingomyelinase 2 Regulating a Signaling Cascade Leading to
1016 Activation of beta1-Integrin. *Cell Physiol Biochem* **51**, 1815-1829.
1017 **Yamaji, A., Sekizawa, Y., Emoto, K., Sakuraba, H., Inoue, K., Kobayashi, H. and Umeda, M.**
1018 (1998). Lysenin, a novel sphingomyelin-specific binding protein. *J Biol Chem* **273**, 5300-6.
1019 **Yeung, T. and Grinstein, S.** (2007). Lipid signaling and the modulation of surface charge
1020 during phagocytosis. *Immunol Rev* **219**, 17-36.
1021 **Yin, X., Zafrullah, M., Lee, H., Haimovitz-Friedman, A., Fuks, Z. and Kolesnick, R.** (2009). A
1022 ceramide-binding C1 domain mediates kinase suppressor of ras membrane translocation. *Cell Physiol*
1023 *Biochem* **24**, 219-30.
1024 **Zhang, Y., Bei, Y., Delikat, S., Bayoumy, S., Xin-Hua, L., Basu, S., McGinley, M., Chan-Hui, P.**
1025 **Y., Lichenstein, H. and Kolesnick, R.** (1997). Kinase suppressor of Ras is ceramide-activated protein
1026 kinase. *Cell* **89**, 63-72.
1027 **Zhao, H., Przybylska, M., Wu, I. H., Zhang, J., Siegel, C., Komarnitsky, S., Yew, N. S. and**
1028 **Cheng, S. H.** (2007). Inhibiting glycosphingolipid synthesis improves glycemic control and insulin
1029 sensitivity in animal models of type 2 diabetes. *Diabetes* **56**, 1210-8.
1030 **Zhao, L., Zhao, J., Zhong, K., Tong, A. and Jia, D.** (2022). Targeted protein degradation:
1031 mechanisms, strategies and application. *Signal Transduction and Targeted Therapy* **7**, 113.
1032 **Zhou, K., Dichlberger, A., Martinez-Seara, H., Nyholm, T. K. M., Li, S., Kim, Y. A.,**
1033 **Vattulainen, I., Ikonen, E. and Blom, T.** (2018). A Ceramide-Regulated Element in the Late
1034 Endosomal Protein LAPTM4B Controls Amino Acid Transporter Interaction. *ACS Central Science* **4**,
1035 548-558.
1036 **Zhou, M., Horita, D. A., Waugh, D. S., Byrd, R. A. and Morrison, D. K.** (2002). Solution
1037 structure and functional analysis of the cysteine-rich C1 domain of kinase suppressor of ras
1038 (KSR)11Edited by P. E. Wright. *Journal of Molecular Biology* **315**, 435-446.

1039

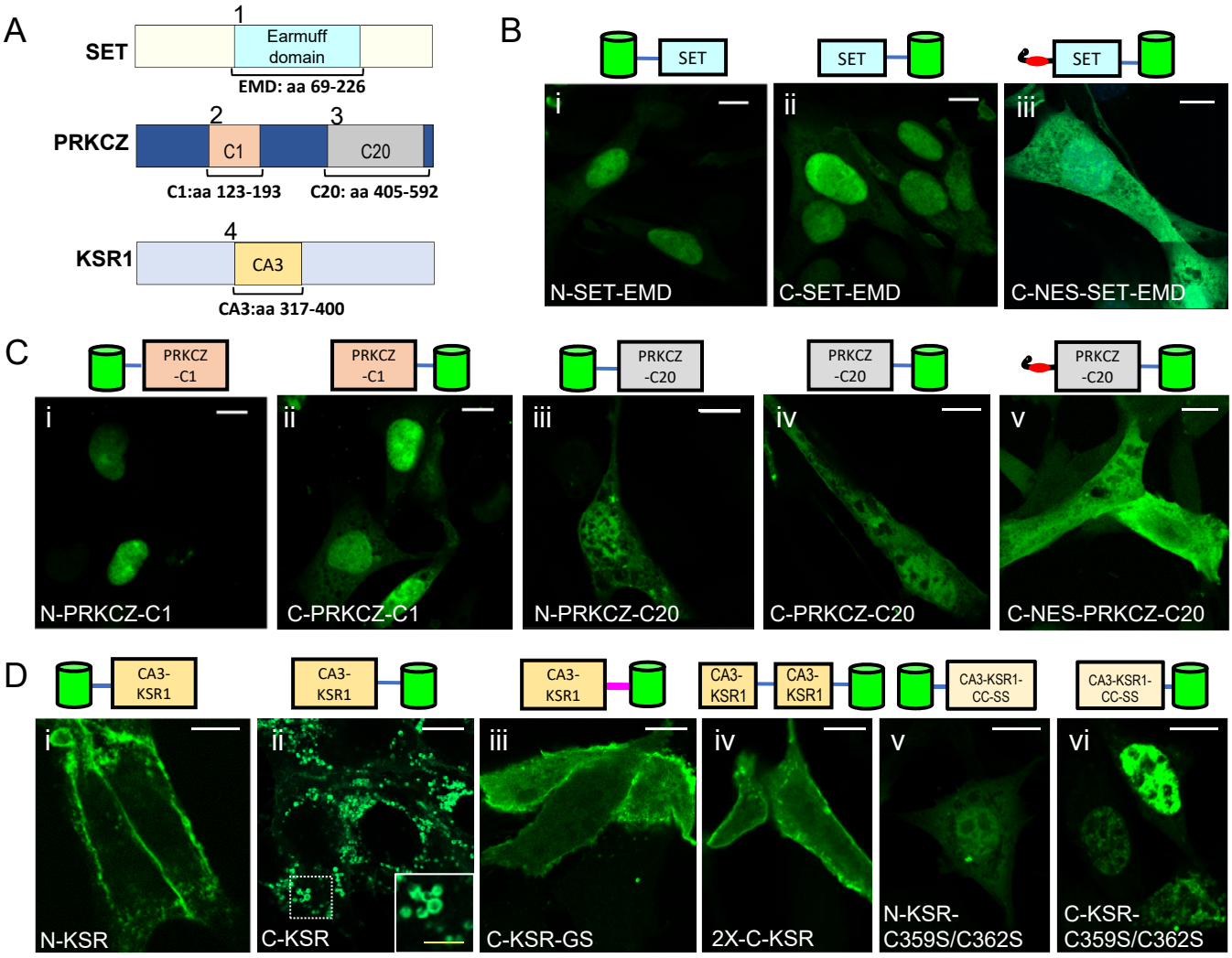

Figure 1. *Localization of candidate ceramide probes in mouse embryonic fibroblasts (MEFs).* **A)** Schematic representation of ceramide-binding domains used for probe construction from the following source proteins: Human SET earmuff domain (EMD), amino acids (as) 69-226; atypical PKC type zeta C1 domain (PRKCZ-C1, aa 123-193) and C20 domain (PRKCZ-C20, aa 405-592); and KSR1 CA3 domain (KSR, aa 317-400). **B-D)** Confocal images of MEF cells transfected with N-terminally (N-) or C-terminally (C-) EGFP-tagged ceramide-binding domains of SET (B), PRKCZ (C) and KSR1 (D). Constructs preceded by a nuclear export signal are labelled NES, the construct bearing a glycine-serine linker is GS, the tandem construct is 2X, and the cysteine mutants are C359S/C362S. The inset in C-KSR highlights enlarged vesicular structures. White bars = 10 µm, yellow bar = 3 µm.

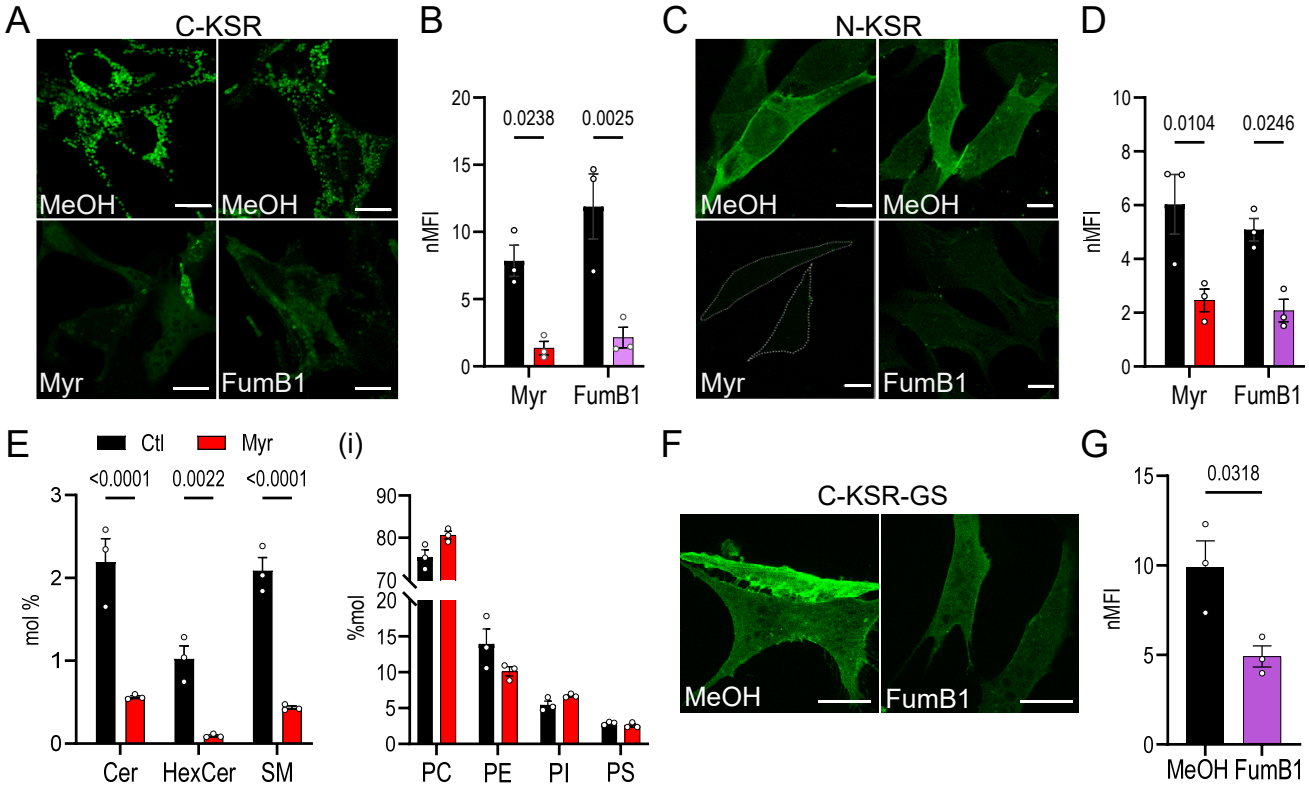

Figure 2. *Response of KSR probes to sphingolipid depletion.* **A-D)** Confocal images of MEF cells stably expressing C-KSR (A) or N-KSR (B) (in green) treated with; 0.5 µM myriocin (Myr) or 2.5 µM fumonisin B1 (FumB1) FumB1 for 3d; and respective methanol (MeOH) vehicle controls. The quantification of the normalized total cellular mean fluorescence intensity (nMFI) of cells in A,C are shown in B, D respectively . (n= 3 coverslips for each condition). White bars = 10 µm. **E)** Targeted lipidomic analysis of MEF cells stably expressing C-KSR, treated with Myr as above. Left panel shows the quantification of the sum total mass of lipids classified as ceramides (Cer), hexosyl-ceramides (HexCer), and sphingomyelins (SM), normalized to the total mass glycerophospholipids in the same sample (expressed as percent mole, %mol). Inset (i) shows the quantification of total major phospholipid species phosphatidylcholine (PC), phosphatidylethanolamine (PE), phosphoinositide (PI), phosphatidylserine (PS). (n=3 independent biological samples, see also Supplementary Data S1). **F-G)** Similar analysis as in (A-D) of cells transiently transfected with C-KSR-GS (green) and treated overnight with 10 µM FumB1 . Bars are means +/- SEM. (n=3 coverslips).

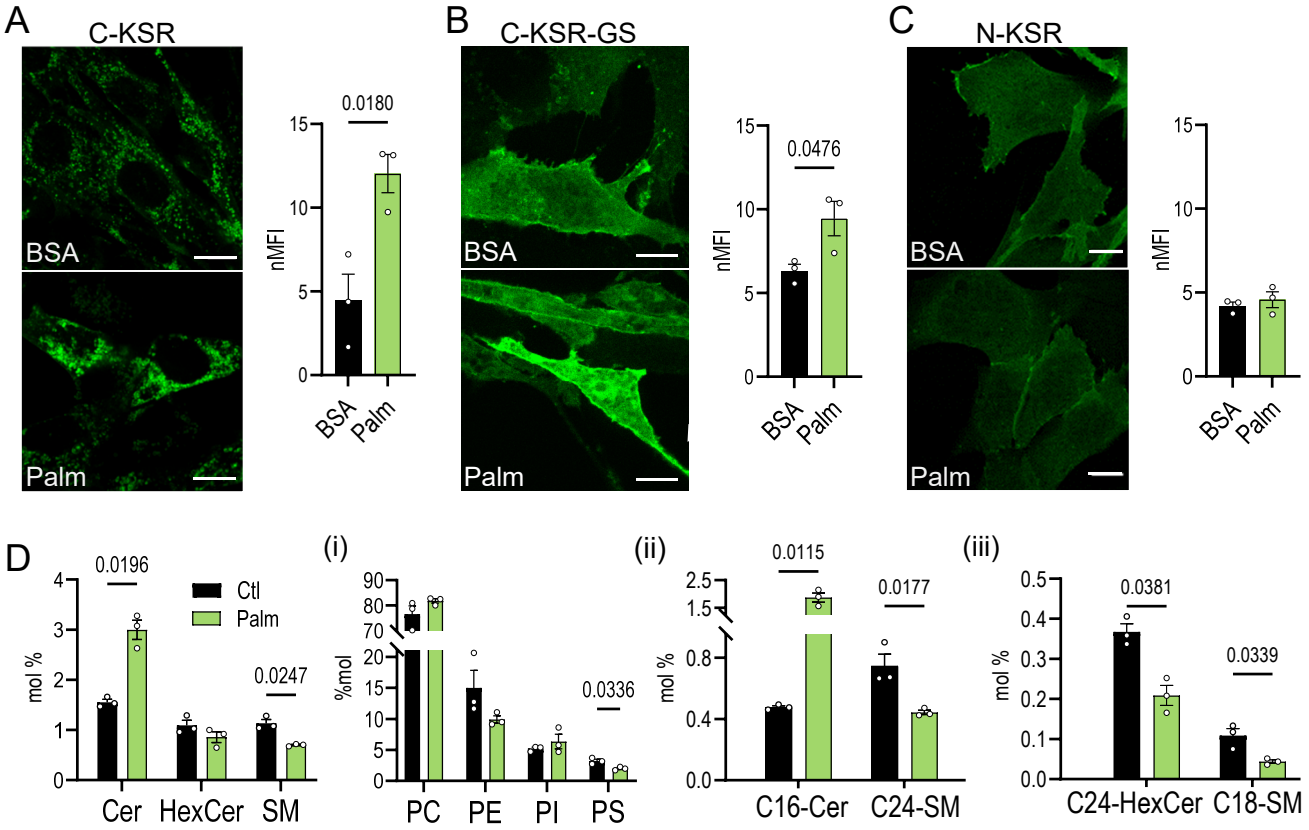

Figure 3. *Response of KSR probes to palmitate-induced ceramide accumulation.* **A-C)** Confocal images of MEF cells expressing C-KSR (A), C-KSR-GS (B) and N-KSR (C) (in green) treated with; 0.5 mM BSA-palmitate (Palm) or BSA control for 4h. The quantification of the total cellular fluorescence (nMFI) is shown to the right of the respective images (n= 3 coverslips for each condition). **D)** Targeted lipidomic quantification of total Cer, HexCer, and SM in MEF cells expressing C-KSR, treated with Palm as above. Inset (i) shows the quantification of PC, PE, PI and PS. Inset (ii) shows quantification of C16-Cer and C24-SM lipid subspecies. Inset (iii) shows quantification of C24-HexCer and C18-SM lipid subspecies (n=3 independent biological samples, see also Supplementary Data S1). Bars are means +/- SEM. (n=3 coverslips). White bars = 10 µm.

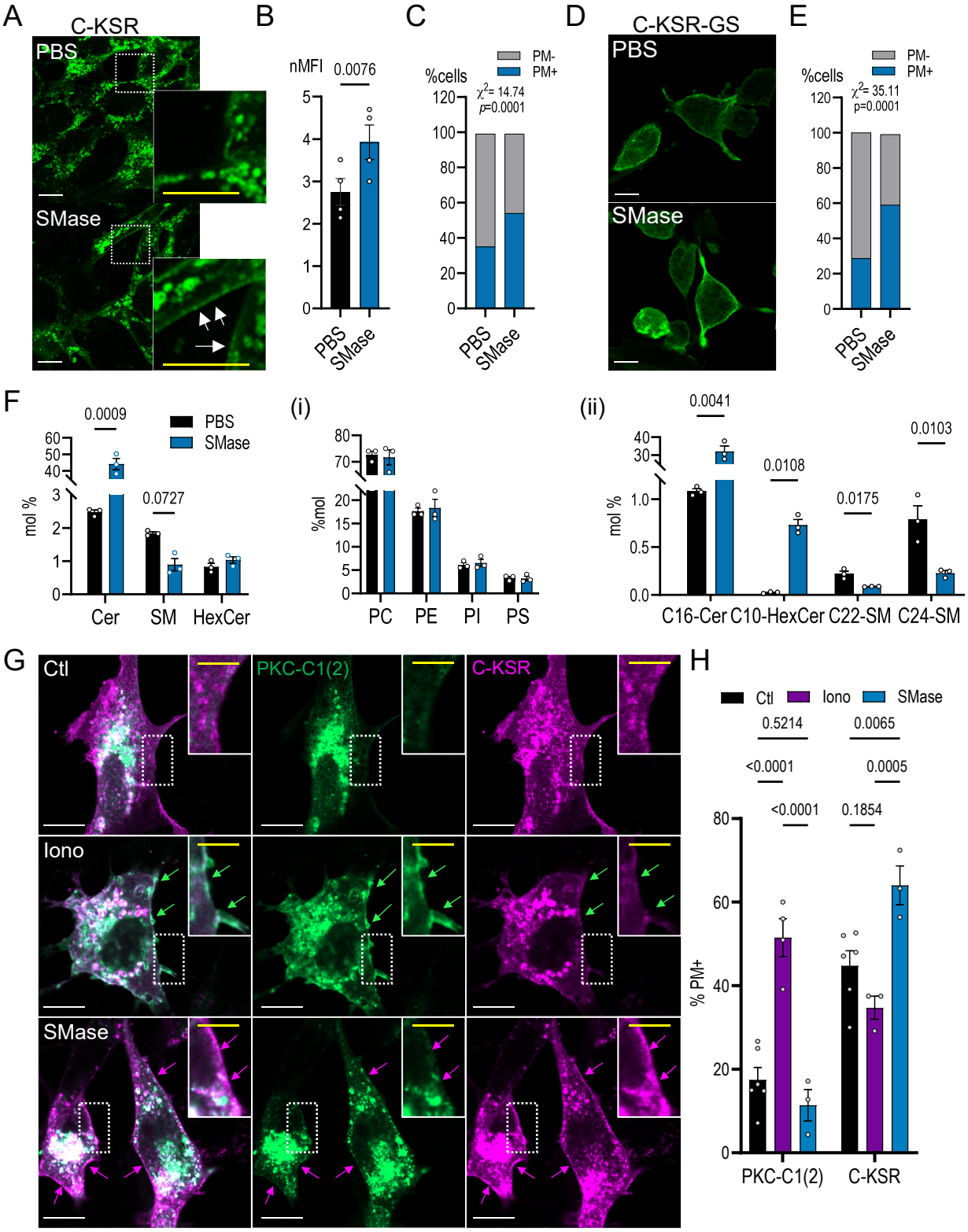

Figure 4. *Response of KSR probes to sphingomyelinase-induced ceramide accumulation.* **A-E)** Confocal images and analysis of C-KSR (A-C) and C-KSR-GS (D-E) in cells treated for 30 min with 0.5 U/ml sphingomyelinase (SMase). In (B) a quantification of total cellular fluorescence (nMFI) is shown, whereas (C) and (E) show quantification of the fraction of cells displaying plasma membrane localization of C-KSR and C-KSR-GS respectively. (n= 4 coverslips) **F)** Targeted lipidomic quantification of total Cer, HexCer, and SM in MEF cells expressing C-KSR, treated with SMase as above. Inset (i) shows the quantification of PC, PE, PI and PS. Inset (ii) shows quantification of C16-Cer, C10-HexCer, C22-SM and C24-SM lipid subspecies. (n=3 independent biological samples, see also Supplementary Data S1). **G-H)** Confocal images of MEF cells co-transfected with C-KSR-mRFP (magenta) and diacylglycerol (DAG) probe PCK-C1(2)-EGFP (green), control (Ctl, top) or treated with 10 μM ionomycin (Iono) for 10 min (middle), or with SMase as above (bottom). G) Quantification of cells in (G) displaying PM localization of either C-KSR or PKC-C1(2) probe. (n= 6/3/3 coverslips for Ctl/Iono/SMase). Bars are means +/- SEM. White bars = 10 μm, yellow bar = 3 μm.

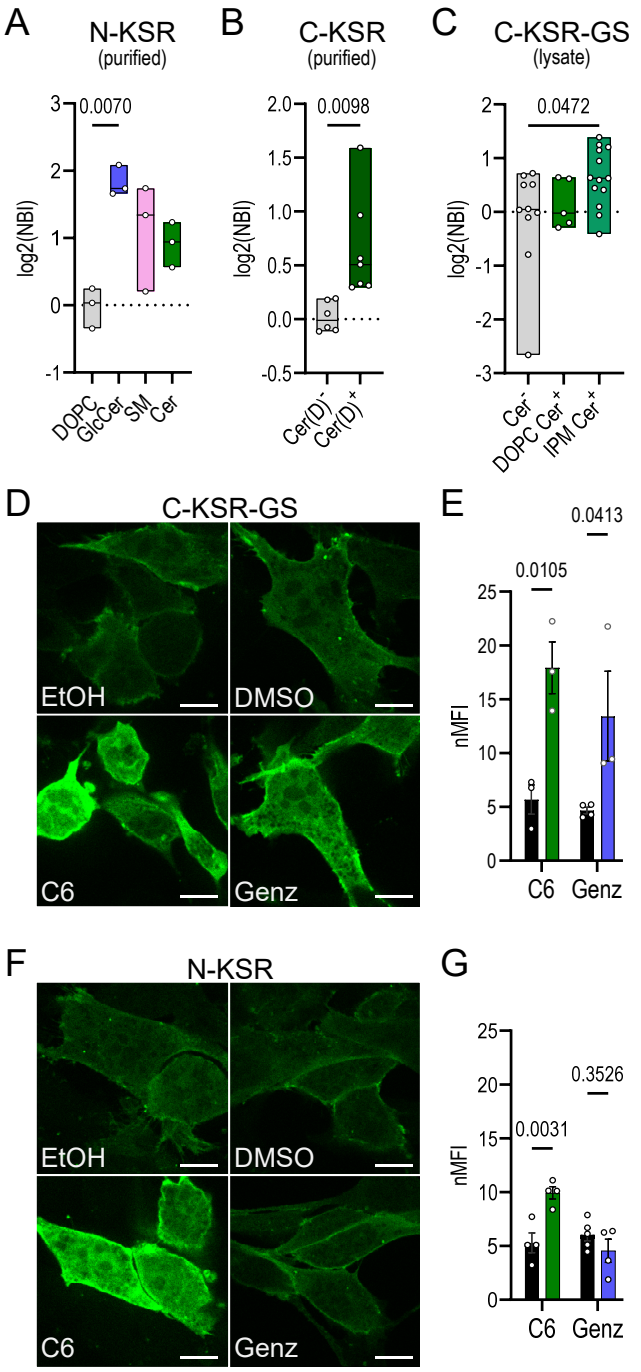

Figure 5. *Differential lipid preference of C- and N-tagged KSR probes.* **A)** Liposome microarray (LiMA) analysis using purified N-KSR. Binding scores of control liposomes containing dioleoyl-phosphatidylcholine (DOPC), and DOPC liposomes containing 2% glucosyl-ceramide (GlcCer), 10% sphingomyelin (SM) or 10% ceramide mixture (Cer) are shown. Binding scores are expressed as log2 transformed normalized binding intensity (NBI) score ratios to control (n = 3 independent biological samples). **B)** LiMA analysis using purified C-KSR. Pooled binding scores of liposomes either lacking ($Cer(D)^-$) or containing ceramide or ceramide derivatives ($Cer(D)^+$). Conditions included were: $Cer(D)^-$: DOPC alone, and 10%PI(4,5)P2 or 10% sphingosine in DOPC. $Cer(D)^+$: 10% ceramide mix (Cer), SM, GlcCer or Cer1P in DOPC. (n=6/7 $Cer(D)^-$/$Cer(D)^+$ independent biological samples). **C)** LiMA analysis of C-KSR-GS lysates pooled binding scores of control liposomes (Cer^-) or containing 5% and 10% ceramides in either a DOPC or inner plasma membrane (IPM) mimicking composition (DOPC Cer^+ and IPM Cer^+, respectively). Conditions included were: Cer^-: DOPC, POPC and IPM control liposomes; DOPC Cer^+: C18-ceramide in DOPC; IPM Cer^+: ceramide mix and C18-ceramide (n = 10/5/13 Cer^-/ DOPC Cer^+/ IPM Cer^+ independent biological samples). **D-G)** Confocal images of MEFs expressing C-KSR-GS (D) or N-KSR (E) and treated (bottom) with either Cer analog C6-ceramide (200 µM, 2h, left) or 100 µM of the GlcCer synthase inhibitor Genz-123346 (Genz, 1d, right), or their respective vehicle controls ethanol (EtOH) or dimethylsulfoxide (DMSO) (top). (F) and (H) show the quantification of total cellular fluorescence (nMFI) of C-KSR-GS and N-KSR respectively (in F: n=3/3/4/3 coverslips for EtOH/C6/DMSO/Genz; in H: n = 4 coverslips for all conditions). In A-C the box plots show the range (min to max) and the line shows the median value. In E,G, the bars are means +/- SEM. White bars = 10 µm.

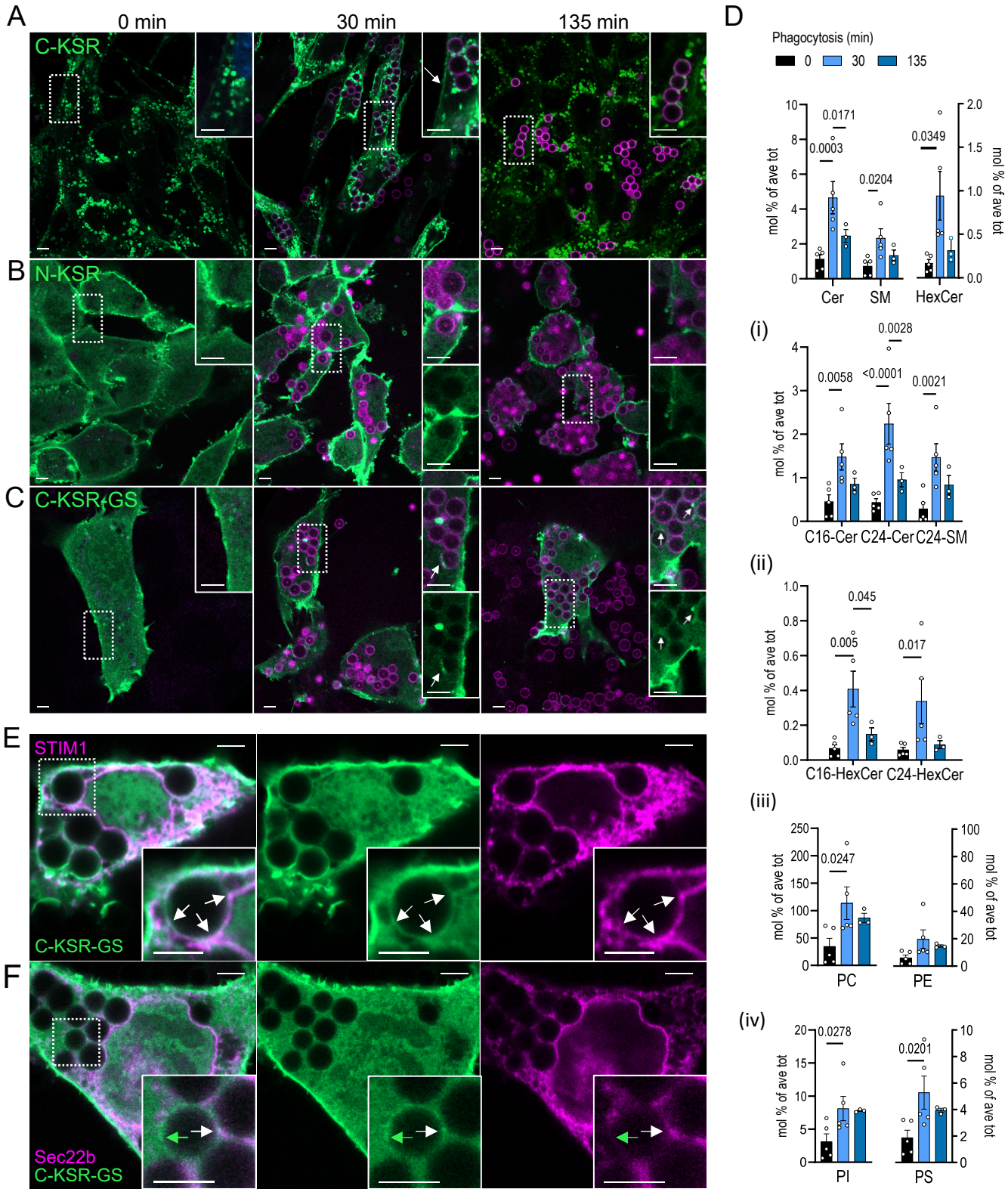

Figure 6. *Behavior of KSR probes during phagocytosis in MEFs.* **A-C)** Confocal images of phagocytic MEFs expressing (in green) C-KSR (A), N-KSR (B) and C-KSR-GS (C), exposed to IgG-Alexa647-coupled beads at 1:10 cell:bead ratio for 0 (left), 30 (middle) and 135 (right) min. **D)** Targeted lipidomic analysis of MEF cells stably expressing C-KSR, treated exposed to IgG-beads as above. Top panel shows the quantification of the sum total Cer, HexCer, SM. Quantification of the species showing significant changes grouped by fatty acid chain length for Cer and (i) or HexCer (ii). Insets (iii) and (iv) show quantification of total phospholipids for PC and PE in (iii), PI and PS in (iV), (n=3 independent biological samples, see also Supplementary Data S1). **E-F)** Confocal images of phagocytic MEFs co-transfected with C-KSR-GS (green) and membrane contact site proteins mCh-STIM1 (E, magenta) and mCh-Sec22b (F, magenta), and exposed to IgG-beads as above. White arrows show periphagosomal regions where overlap of fluorescent protein signal is discerned, green arrow shows regions with green fluorescence only. Bars are means +/-SEM. White bars = 3 µm.

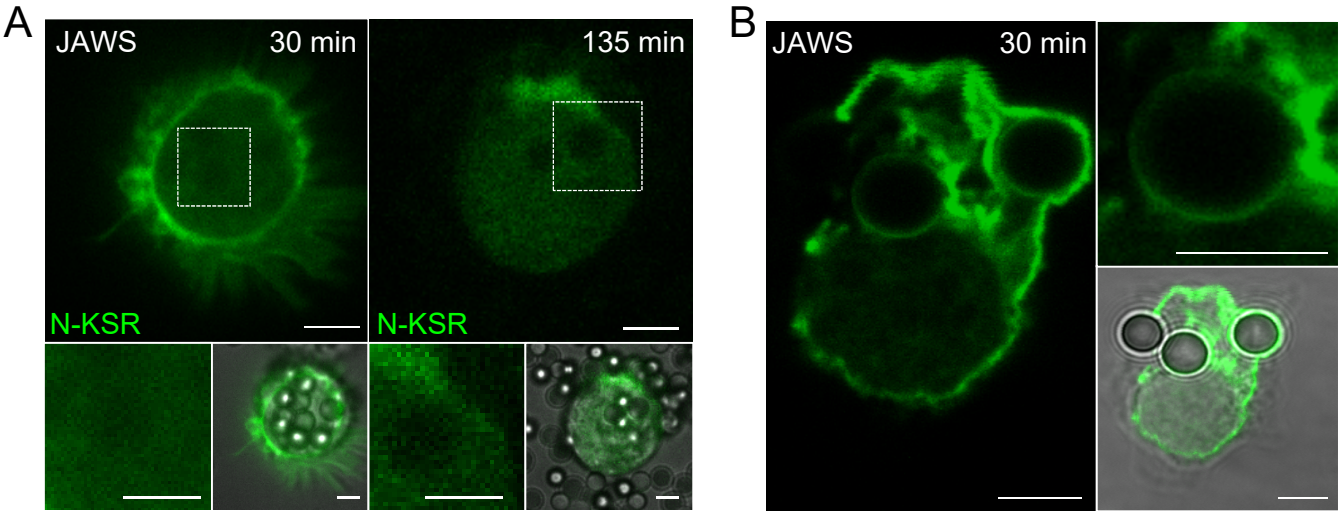

Figure 7. *Behavior of KSR probes during phagocytosis in dendritic cells.* **A-B)** Confocal images of dendritic cell line JAWS transfected with (in green) N-KSR (A) exposed to IgG-coupled beads at 1:10 cell:bead ratio for 30 (left) and 135 (right) min, and C-KSR-GS (B) exposed to beads for 30 min. Brightfield images are shown to confirm presence of internalized beads. Bars = 3 µm.

A

	Fum	*Myr*	*Palm*	*SMase*	*C6*	*Genz*
Cer	↓[1]	↓	↑↑	↑↑↑	↑↑↑[2,3]	↑↑[4]
SM	↓[1]	↓	↓	↓	(↑)[2]	=[4]
HexCer	↓[1]	↓	↓ (C24)	↑ (C10)	↑↑[3]	↓[4]
Phospholipids	↑ (PE)[1]	=	↓ (PS)	=	=[3]	?
N-KSR	↓	↓	=	n.d.	↑	=
C-KSR	↓	↓	↑	↑	tox	n.d.
C-KSR-GS	↓	tox	↑	↑ (PM)	↑↑	↑↑

B

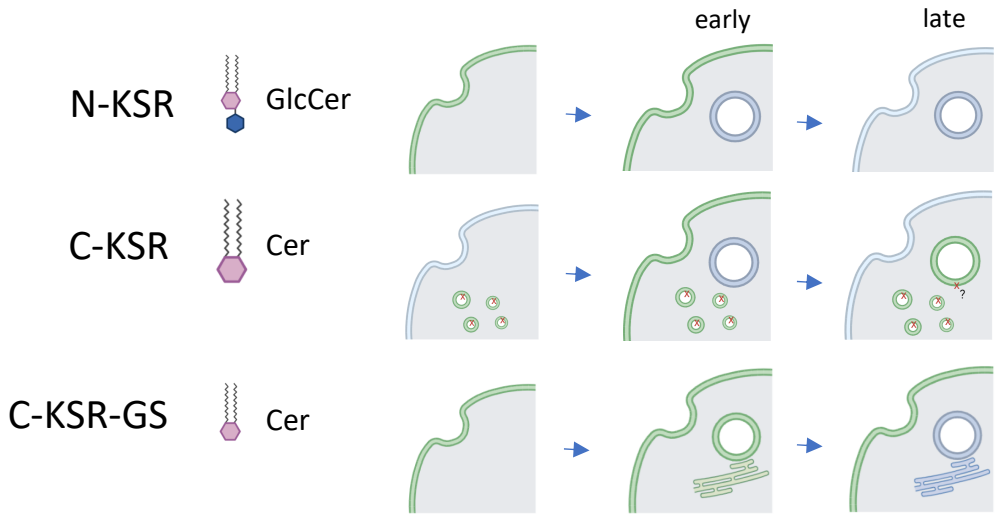

Figure 8. *Summary and model.* **A)** Table summarizing effect of ceramide-modifying treatments used in this study on major lipid classes (ceramides (Cer), sphingomyelins (SM), hexosyl-ceramides (HexCer) and phospholipids) and on the 3 KSR1-based probes. In cases where only certain sub-species of lipids were affected, the major sub-species affected in listed in brackets. Decreases are shown as a red arrow pointing down, increases as green arrow(s) pointing up, and similar levels as an orange equal sign. Tox = toxicity. n.d. = not determined. PM = plasma membrane. Myr (myriocin), Palm (palmitate) and SMase (sphingomyelinase) effects were measured in this study. The effects of Fum (fumonisin B1), C6 (C6-ceramide) and Genz (Genz-123346) are extrapolated from the literature. ([1]Merrill et al, 2011; [2]Vieu et al, 2002; [3]Duran et al. 2012; [4]Koike et al, 2019). **B)** Hypothetical model of the behavior of N-KSR, C-KSR and C-KSR-GS before and during phagocytosis. N-KSR (top), with a higher sensitivity for glucosyl-ceramides (GlcCer) is lost at later stages of phagocytosis. C-KSR (middle) and C-KSR-GS (bottom) are both more sensitive to ceramides (Cer). Higher dynamic range and turnover of C-KSR may help more sensitive detection of ceramide changes at the plasma membrane during early stages of phagocytosis, but presence in lysosomes and phagosomes may represent a partially degraded probe. The more homogeneous and higher cytosolic expression of C-KSR-GS may make it most suitable for detecting ceramide changes on the cytosolic leaflet of organellar membranes such as the phagosome and endoplasmic reticulum. Created with BioRender.com